Transportation Consortium of South-Central States

Tran-SET

Solving Emerging Transportation Resiliency, Sustainability, and Economic Challenges through the Use of Innovative Materials and Construction Methods: From Research to Implementation

Integrated Health Monitoring and Reinforcement of Transportation Structures with Optimized Low-Cost Multifunctional Braided Cables

Project No. 17STTAM04

Lead University: Texas A&M University

Preserving Existing Transportation Systems

Final Report

December 2018

Disclaimer

TECHNICAL DOCUMENTATION PAGE

1. Project No. 17STTAM04	**2. Government Accession No.**	**3. Recipient's Catalog No.**

4. Title and Subtitle Integrated Health Monitoring and Reinforcement of Transportation Structures with Optimized Low-Cost Multifunctional Braided Cables	**5. Report Date** Dec. 2018 **6. Performing Organization Code**
7. Author(s) PI: Ibrahim Karaman https://orcid.org/0000-0001-6461-4958 Co-PI: Darren Hartl https:/orcid.org/0000-0001-9922-0481	**8. Performing Organization Report No.**
9. Performing Organization Name and Address Transportation Consortium of South-Central States (Tran-SET) University Transportation Center for Region 6 3319 Patrick F. Taylor Hall, Louisiana State University, Baton Rouge, LA 70803	**10. Work Unit No. (TRAIS)** **11. Contract or Grant No.** 69A3551747106
12. Sponsoring Agency Name and Address United States of America Department of Transportation Research and Innovative Technology Administration	**13. Type of Report and Period Covered** Final Research Report May 2017 – May 2018 **14. Sponsoring Agency Code**

15. Supplementary Notes

Report uploaded and accessible at: [Tran-SET's website (http://transet.lsu.edu/)](http://transet.lsu.edu/)

16. Abstract

The objective of this research study is to design, fabricate, and characterize multifunctional high strength and self-sensing braided cables and structures using novel Fe-based shape memory alloys (SMAs). The system exploits unique properties of recently developed low-cost super-elastic FeMnAlNi SMAs, which enables excellent super-elastic properties, high strength, and self-sensing in structural health monitoring (SHM) systems. This novel material technology can be coupled with modeling efforts that allow for accurate prediction of both the materials and structural response during sensing. At the conclusion of the project, we have demonstrated that with careful design of processing parameters, it is possible to control the yield strength and superleastic properties of FeMnAlNi SMAs. We have fabricated, for the first time in the world, a large diameter wires and bars from these inexpensive iron based SMAs which are expected to help with scaling up the fabrication of these materials. In addition, we were able to develop a method for fabricating braided cables from the fabricated Fe-SMA wires and a lab scale experimental setup has been designed and built. Prototype design for the braiding weave was created and tested. Finally, an experimental setup has been designed and manufactured to measure changes in the magnetic response of the SMA braided cables under load in order to directly correlate the magnetic response with deflection and strain. Clearly, the successful fabrication of wires and braided cables of the inexpensive iron based SMAs with superelastic strains comparable to nickel-titanium SMAs and with favorable magnetic sensing capabilities have significant implications for transportation infrastructure as these materials can provide structural health monitoring capability while also mitigating large shape changes during natural disasters. Future work needs to focus on revealing the coupling between mechanical properties (in particular damage) and the changes in magnetic properties in order to provide guidance on how these materials can be utilized in structural health monitoring.

17. Key Words Shape Memory Alloys, Braided Cables, Structural Optimization, Health Monitoring, Multifunctional Materials, Magnetic Sensing	**18. Distribution Statement** No restrictions

19. Security Classif. (of this report) Unclassified	**20. Security Classif. (of this page)** Unclassified	**21. No. of Pages** 39	**22. Price**

Form DOT F 1700.7 (8-72) **Reproduction of completed page authorized.**

SI* (MODERN METRIC) CONVERSION FACTORS

APPROXIMATE CONVERSIONS TO SI UNITS

Symbol	When You Know	Multiply By	To Find	Symbol
LENGTH				
in	inches	25.4	millimeters	mm
ft	feet	0.305	meters	m
yd	yards	0.914	meters	m
mi	miles	1.61	kilometers	km
AREA				
in^2	square inches	645.2	square millimeters	mm^2
ft^2	square feet	0.093	square meters	m^2
yd^2	square yard	0.836	square meters	m^2
ac	acres	0.405	hectares	ha
mi^2	square miles	2.59	square kilometers	km^2
VOLUME				
fl oz	fluid ounces	29.57	milliliters	mL
gal	gallons	3.785	liters	L
ft^3	cubic feet	0.028	cubic meters	m^3
yd^3	cubic yards	0.765	cubic meters	m^3
	NOTE: volumes greater than 1000 L shall be shown in m^3			
MASS				
oz	ounces	28.35	grams	g
lb	pounds	0.454	kilograms	kg
T	short tons (2000 lb)	0.907	megagrams (or "metric ton")	Mg (or "t")
TEMPERATURE (exact degrees)				
°F	Fahrenheit	5 (F-32)/9 or (F-32)/1.8	Celsius	°C
ILLUMINATION				
fc	foot-candles	10.76	lux	lx
fl	foot-Lamberts	3.426	candela/m^2	cd/m^2
FORCE and PRESSURE or STRESS				
lbf	poundforce	4.45	newtons	N
lbf/in^2	poundforce per square inch	6.89	kilopascals	kPa

APPROXIMATE CONVERSIONS FROM SI UNITS

Symbol	When You Know	Multiply By	To Find	Symbol
LENGTH				
mm	millimeters	0.039	inches	in
m	meters	3.28	feet	ft
m	meters	1.09	yards	yd
km	kilometers	0.621	miles	mi
AREA				
mm^2	square millimeters	0.0016	square inches	in^2
m^2	square meters	10.764	square feet	ft^2
m^2	square meters	1.195	square yards	yd^2
ha	hectares	2.47	acres	ac
km^2	square kilometers	0.386	square miles	mi^2
VOLUME				
mL	milliliters	0.034	fluid ounces	fl oz
L	liters	0.264	gallons	gal
m^3	cubic meters	35.314	cubic feet	ft^3
m^3	cubic meters	1.307	cubic yards	yd^3
MASS				
g	grams	0.035	ounces	oz
kg	kilograms	2.202	pounds	lb
Mg (or "t")	megagrams (or "metric ton")	1.103	short tons (2000 lb)	T
TEMPERATURE (exact degrees)				
°C	Celsius	1.8C+32	Fahrenheit	°F
ILLUMINATION				
lx	lux	0.0929	foot-candles	fc
cd/m^2	candela/m^2	0.2919	foot-Lamberts	fl
FORCE and PRESSURE or STRESS				
N	newtons	0.225	poundforce	lbf
kPa	kilopascals	0.145	poundforce per square inch	lbf/in^2

TABLE OF CONTENTS

LIST OF FIGURES

ACRONYMS, ABBREVIATIONS, AND SYMBOLS

FEA	Finite Element Analysis
GMR	Giant Magneto-Resistive
MSMA	Magnetic Shape Memory Alloy
SHM	Structural Health Monitoring
SMA	Shape Memory Alloy
XFEM	Extended Finite Element Method

EXECUTIVE SUMMARY

The objective of this collaborative research is to design, fabricate, and characterize multifunctional high strength and self-sensing braided cables and structures using novel Fe-based shape memory alloys (SMAs). Concrete structures with embedded Fe-SMA wires and cables are expected to exploit unique properties of recently developed low-cost super-elastic FeMnAlNi SMAs, which enable excellent super-elastic properties, high strength, and self-sensing in structural health monitoring (SHM) systems. This novel material technology can be coupled with modeling efforts that allow for accurate prediction of both the materials and structural response during sensing. Through a combined approach of structural optimization and materials design, this research aims at simultaneously achieving advantageous mechanical properties and self-monitoring capabilities in a single material for transportation structures.

During this project, important development and impacts have been made in areas of both materials/cable development and modeling. In materials/cable development, a method has been successfully demonstrated that allows for the fabrication of large diameter wires from Fe-SMA. Additionally, a method for the fabricating braided cables from Fe-SMA wires has been identified and an experimental setup has been developed. Prototype design for the braiding weave was created and tested. For measuring changes in the magnetic response of the braided cable under load directly correlate with deflection and strain, an experimental setup has been built.

For modeling, the combination of wire-concrete cohesion and crack propagation are likely to improve the accuracy of current modeling techniques of reinforced concrete structures. An Abaqus model was created to show how the solid mechanics of a crack propagating past a magnetic shape memory alloy (MSMA) wire led to a noticeable local phase transformation. The MSMA wire near the crack tip transforms under significant loading into martensite, allowing for external sensing using a permanent magnet and sensor pair to measure magnetic flux change. Applying this technique to a current reinforced concrete model would only add to its validity, considering an interaction property rarely modeled. The main goal, magnetic damage detection, is likely to be a great contribution to fields involving concrete structures. It is expected to allow the detection of inner damage, difficult to be seen from the exterior of the structure. This capability is extremely useful in determining the lifespan, durability, and safety of a concrete structure.

IMPLEMENTATION STATEMENT

As the project enters the implementation phase, the primary goal is to show that the strain in the wires and braided Fe-SMA cable directly correlates with changes in its magnetic response and can be converted into structural deflections using simple instruments. Another implementation objective is to simulate and predict with high accuracy the change in the magnetic response using a finite element model. The authors have completed the prerequisites work for this demonstration including full characterization of the Fe-SMA wire response, design, and fabrication of the magnetic sensing setup, and creation and validation of the coupled finite element model that is able to predict both the super-elastic response of the Fe-SMA as well as the magnetic sensing response. The focus of the implementation phase will be to demonstrate the sensing capabilities of the Fe-SMA cable both in a stand-alone form.

The authors have established an industrial collaboration with Fort Wayne Metals, one of the leading metal cable and braided structure producers in the United States. Fort Wayne metals have agreed to provide in-kind support of materials and personnel time to co-develop the Fe-SMA toward a commercial product.

1. INTRODUCTION

To enhance the longevity and performance of next generation transportation structures, high performance material and systems can be integrated with health monitoring systems to obtain real time data on the condition of structures and identify defects in a timely fashion. One of the potential solutions to this is the integration of multifunctional materials. The use of multifunctional materials in transportation structures can provide simultaneous sensing capabilities with simplified designs, improved load bearing capacity, reduced material use, and less manufacturing complexity. A particularly appealing and interesting class of multifunctional materials is shape memory alloys (SMAs). Super-elastic SMAs can produce large recoverable deformations as a result of reversible phase transformation, which is triggered by change in stress/strain.

A relatively new field of exploration for structural health monitoring (SHM) is non-destructive evaluation via magnetic sensing, evaluating the external magnetic fields around structural components. Magnetic shape memory alloys (MSMAs), known for their ability to change properties with their respective phase changes, can alter magnetic fields due to their change in magnetic permeability in the presence of internal stress. This use of magnetic sensing for non-destructive evaluation represents an inherently multidisciplinary research area with respect to both the computational and experimental domain.

In recent years, a FeMnAlNi SMA showing large full-recoverable super-elasticity and high strength was engineered that could address the simultaneous need of excellent mechanical response and low cost *(1–3)*. This Fe-SMA contains inexpensive alloy elements and does not require high vacuum during melting required for titanium-based alloys like NiTi. Furthermore, the Fe-SMA shows an interesting meta-magnetic shape memory response, where the magnetic characteristics of the alloy change significantly between the austenite and martensite phases. The result is a change in the induced magnetization of the material during phase transformation, for example from applied stress, which can be easily detected using commercial magnetometers. This property can be harnessed to create a method to monitor the stresses and strains on structural systems with Fe-SMAs remotely and in a non-destructive fashion. The combination of these properties enables a new kind of SHM framework where the structural and sensing elements are integrated, and quantitative information could be collected in real-time with simple instruments.

1.1. Background

1.1.1. Iron-based Shape Memory Alloys

Currently, the most widespread SMAs are based on NiTi, or “nitinol”. While they show excellent super-elastic properties, their high cost severely limits their application in large-scale applications in transportation projects. Recently, inexpensive FeMnAlNi SMA have been developed showing large full-recoverable super-elasticity and high strength. Specifically, the recent introduction of a magnetic $Fe_{43.5}Mn_{34}Al_{15}Ni_{7.5}$ (FMAN) SMA *(1, 9–11)* has provided solution to the poor loadbearing capabilities in MSMAs. This material demonstrates a combination of meta-magnetic shape memory effect and robust mechanical properties suitable for structural applications. The authors have successfully produced the material in polycrystalline form and demonstrated tensile strength over 800 MPa and ductility exceeding 10% strain, making it one of the first MSMAs capable of exhibiting simultaneous self-sensing and self-centering when applied in an infrastructure system *(1)*. Of particular interest of the FMAN alloy is that super-elasticity is observed in a wide temperature range from -150 to +150°C *(1)*. This property is crucial for the practical use of such materials in infrastructures since the self-centering capabilities of the material would remain unaffected by the ambient temperature, and the technology can be used without modifications in both very hot and very cold climates.

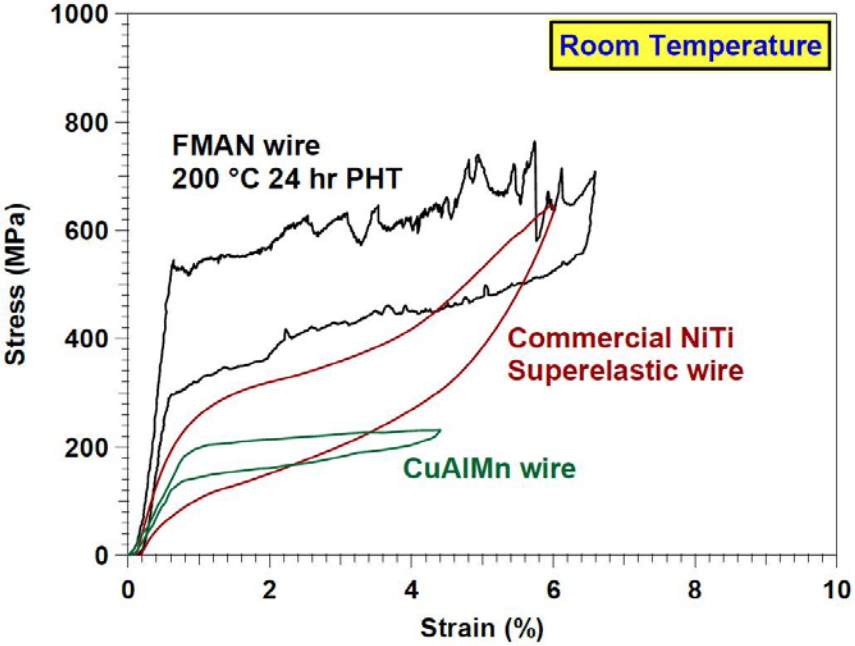

Figure 1. Comparison of the super-elastic response of a FMAN wire with a conventional NiTi, and a CuAlMn SMA.

The authors have performed systematic studies on the processing and physical metallurgy aspects of the $Fe_{43.5}Mn_{34}Al_{15}Ni_{7.5}$ SMA and have published a number of papers on these topics *(9–15)*. Through a combination of precipitation hardening and grain size control techniques developed by the authors *(11, 15)*, we have demonstrated high-strength FMAN polycrystalline wires showing large and fully reversible super-elastic strains near 7%. Figure 1 shows the stress-strain response of a FMAN wire with 24 hour precipitation heat treatment at 200 °C. Compared to a conventionally processed nickel-rich NiTi super-elastic alloy, the FMAN SMA shows a similar strength level and comparable level of transformation strain and energy dissipation (stress hysteresis) while exhibiting somewhat higher initial stiffness. On the other hand, both FMAN and NiTi are significantly stronger than CuAlMn SMAs, and possess the ability to dissipate larger amount of energy per cycle. It is worth noting that the transformation stress level of the FMAN SMA can be easily increased or decreased by changing duration of the precipitation heat treatment at 200 °C. For example, the 24-hour heat-treated case shown in Figure 1 produces a high transformation stress of 520 MPa. However, a lower transformation level may be desired in order to allow the self-centering response to trigger at lower deformation levels, for example where a transformation stress level of 400 MPa is obtained when the heat treatment at 200 °C is shortened to 3 hours.

1.1.2. Structural Braided Cable Design

Given the expense involved in the experimental design-build-test-redesign cycles, the determination of optimal cable configurations for embedding into structural matrices such as concrete require the ability to accurately analyze the same. Fortunately, the modeling of such structures has a long history, with cables *(12)* and meshes *(13)* having been considered for some time. Researches into novel architectures such as woven tubes *(14)* also continue to this day, and where possible these past developments are leveraged toward the current work. However, experimental studies *(15, 16)* have shown that the response of SMA cables is quite complex, and that local highly nonlinear transformation effects dominate the response. Therefore, rigorous numerical approaches such as finite element analysis (FEA), and multi-scale implementations of the same, are required for the current effort.

The PIs have computationally analyzed various wire-based structural architectures formed from various SMA materials, and in particular have considered the fully coupled thermo-mechanical response of these materials using both FEA and other lower fidelity but less computationally expensive approaches. For example, novel implementations of the underlying constitutive models have been formulated and demonstrated for woven meshes in which any arbitrary planar arrangement of active wires can be considered, including tri-weaves, etc., in a computationally efficient manner *(16)*. This can be very effective for the macroscopic design of weaves as embedded into a structural matrix. Example meshes considered are shown in Figure 2a.

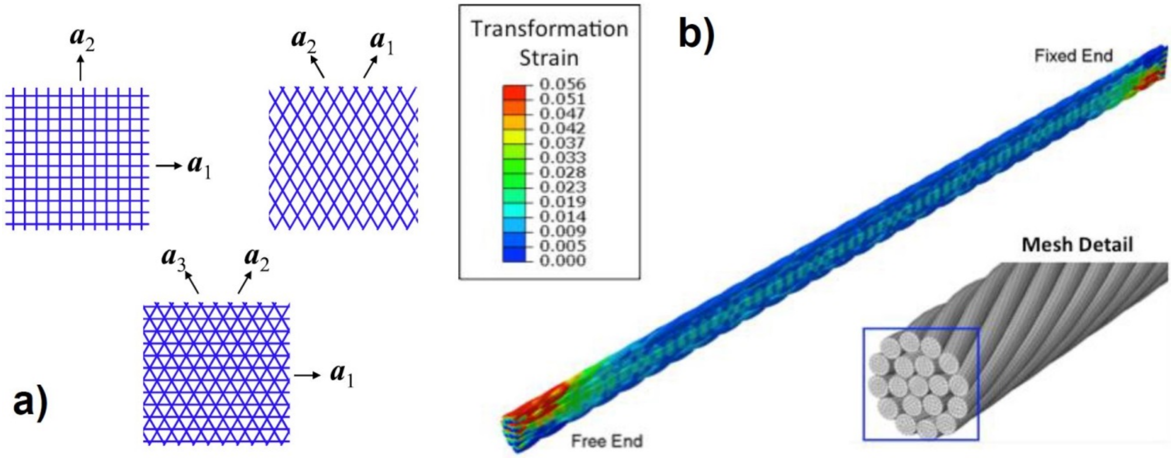

Figure 2. Examples of previous SMA wire-based architectures considered for analysis by the PIs, including: a) a wide range of SMA meshes analyzed at the macrostructural scale *(16)* and b) twisted cables analyzed at the local scale *(17)*.

The consideration of local phase transformation effects in woven, twisted, and braided architectures is much more difficult and requires computationally intensive analysis. Local interactions between individual wires are inherently three-dimensional, and the complex multiaxiality of various shape memory responses must be carefully considered using 3-D constitutive model implementations *(18, 19)*. Even more difficult to analyze, however, is the widespread contact occurring between individual wire components. Such highly non-linear analysis requires the use of explicit methods, for which the modeling methods of the authors have been recently adapted. Using this approach, such complex effects as the bending response of a twisted SMA wire-based cable have now been analyzed *(20)*. Figure 3 shows the distributed phase transformation strain generated in such a cable under bending. Axial deformations of the type expected in a concrete reinforcement application are slightly easier to analyze, though the calculation of magnetization changes adds complexity.

Finally, success of the our efforts requires not only the ability to consider the local transformation effects of complicated SMA wire configurations but also the ability of these effects to be sensed for the purposes of damage location. We have worked to develop schema for sensing stress concentrations due to damage *(8, 20)*. It was shown that SMA bodies nearer localized damage produced a strengthened transformation response, and that the combination of multiple such signals, even assuming a relatively sparse distribution of particles, could be used to pinpoint damage with good accuracy *(20)* (Figure 3).

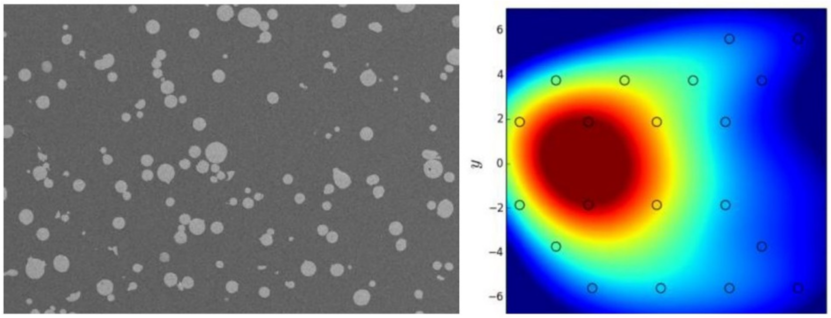

Figure 3. Example distributions of phase transforming SMA particles in an aluminum matrix and developed computational design scheme for optimally distributing such particles to best locate damage *(20)*.

1.1.3. Strain-Sensing Through Meta-Magnetic Shape Memory Response

When martensitic phase transformation or variant reorientation is induced through stress under an external magnetic field, the magnetization level, and thus the magnetic flux, of MSMAs changes noticeably. This change can easily be detected through a magnetometer. Since the magnitude of the change in magnetization is directly proportional to the amount of material transformed or reoriented variants, which is related to the super-elastic or shape memory strain, the quantitative change in magnetization under stress could be used to determine the strain of the material. This is the capability that enables self-sensing properties of MSMAs.

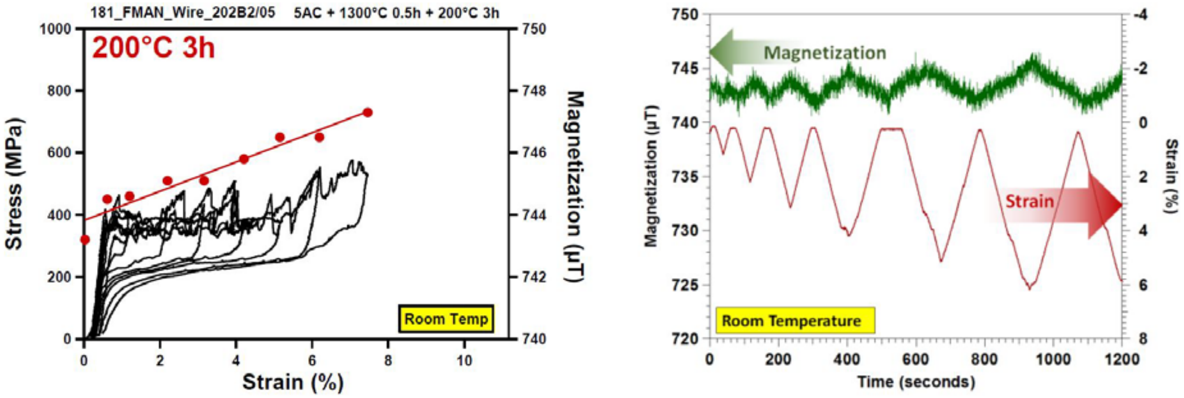

Figure 4. (a) Magneto-mechanical response of FMAN wire after 3 hour precipitation heat treatment: the red dots above the stress-strain curve shows the maximum magnetization in the wire measured at a given applied strain level, and (b) time history comparison of magnetization and strain during loading cycles of part a.

FeMnAlNi SMA demonstrates the meta-magnetic shape memory behavior: Figure 4a shows the relationship between applied strain on the FeMnAlNi wire and the maximum magnetization. A biasing magnetic field of 500 gauss was applied through a permanent magnet on the FeMnNiAl wire by adjusting the strength of the magnet and the distance between the magnet and the wire. The magnetic signal was monitored using a thin film magnetometer (Xtrinsic MAG3110) typically found in smartphones. When the composite was pulled in tension and stress-induced phase transformation occurred, the maximum measured magnetization was altered as the martensite phase, which has a different magnetic character from the austenite, is formed. When the material was unloaded, the magnetization returned to the initial value as martensite reverted back to austenite. This means that the change in magnetization can be directly correlated with strain in the wire. The time history comparison of the magnetization changes during the cyclic load-unloading process is shown in Figure 4b.

2. OBJECTIVE

The objective of this research project was to design, fabricate, and characterize multifunctional high-strength and self-sensing braided cables using novel Fe-based SMAs. To achieve this objective, the study was divided into five specific tasks:

2.1. Design, Fabrication, and Characterization (Technical)

1. Design the optimized braided cable configuration that maximizes the load-bearing capabilities and super-elastic response of the Fe-SMA wires.
2. Design the embedding strategy of cables in structural composites for crack detection.
3. Fabricate braided cables of Fe-SMAs.
4. Characterize the mechanical response of the braided cable bundle and validate design optimization.

2.2. Demonstration of SHM Capability (Implementation)

5. Demonstrate that changes in the magnetic response of the braided cable under load directly correlate with deflection and strain for SHM.

3. SCOPE

The scope of the proposed work includes all experiments and modeling effort designed to achieve the demonstration of the self-sensing Fe-SMA technology in a context relevant to transportation infrastructure. The demonstration took place during the implementation phase of the project, while the research portion of the project concerned with design and fabrication of the cables, the magnetic measurement instrumentations, and models that predict the response of both the material and its use as cable reinforced concrete structure. The scope of the work does not cover basic development of new model types, but rather applies existing well-calibrated model to the application. The work also does not cover basic metallurgical development or improvement of the Fe-SMA alloy, but rather includes techniques that allow the properties of the material to be properly tailored to the application needs.

4. METHODOLOGY

In this section, the experimental and computational methods used in the project and those and specifically developed for the project are discussed in detail. In order to fabricate braided cables of Fe-SMAs using polycrystalline wires, detailed thermomechanical processing steps required to produce them are reported. Methods to induce abnormal grain growth to eliminate grain boundary constrains are explained. To characterize mechanical behavior of the wires and cables, new grip designs that help to increase the contact area between large diameter cables and wires are demonstrated. Finally, methodologies for embedding cables in structural composites for crack detection are discussed.

4.1. Fabrication of Braided Cables of Fe-SMAs

Fe-SMA alloy with a nominal composition of Fe-34%Mn-15%Al-7.5%Ni at.% was used in this study. In the following sections, thermomechanical processing and abnormal grain growth methods are explained in detail to fabricate superelastic Fe-SMA alloy wires and cables.

4.1.1. Thermomechanical Processing to Produce Polycrystalline Fe-based SMA

To enable wire drawing of the FeMnAlNi at room temperature, it is necessary to create a two-phase microstructure consisting of a ductile second phase with a face centered cubic (fcc) crystal structure along with matrix phase with a body centered cubic (bcc) crystal structure. In order to generate this microstructure, the authors have developed thermomechanical processing steps given in Figure 5 as represented in the blue region. Firstly, ingots were prepared by vacuum induction melting and hot extruded at 1,000 °C with an area reduction of 7:1. The resulting rods were then solution heat treated at 1,200 °C and annealed at 900 °C for 30 min under high purity argon atmosphere and followed by water quenching. This step was performed to introduce a high-volume fraction of ductile second phases necessary for wire drawing at room temperature. The heat-treated rod then cold-drawn into wire with a final diameter of 0.5 mm. Total cold-work in the wires are 75%. After thermomechanical processing, composition of the wires were determined using Wavelength Dispersive Spectroscopy (WDS) and variations from nominal composition (Fe-34%Mn-15%Al-7.5%Ni at. %) are found to be less than 0.2%.

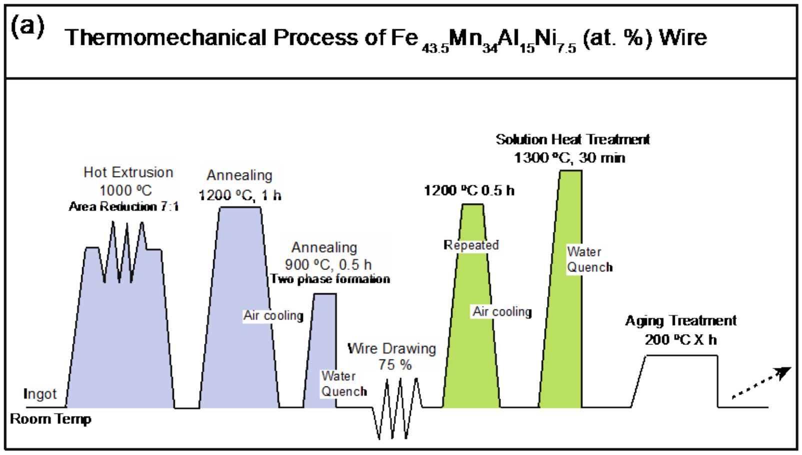

Figure 5. Thermomechanical processing history of Fe-34%Mn-15%Al-7.5%Ni (at. %) super-elastic wire.

4.1.2. Method to Induce Abnormal Grain Growth

Fe-based shape memory alloys usually suffer from large elastic and transformation strain anisotropy. This leads to high internal stresses between grains with large orientation mismatches during martensitic transformation. Additionally, limited number of martensite variants in Fe-based systems inhibits strain accommodation at the grain boundaries and intergranular fracture occurs before the transformation is complete.

Therefore, it is necessary to eliminate grain boundary constraints, triple junctions to obtain good super-elasticity. In order to eliminate these constraints, grain size of the material has to be coarse, perpendicular to the wire axis and span the cross section of the wire. The authors have developed a simple technique to obtain large grain size through abnormal grain growth. In this method, material has to be repeatedly cycled between single phase and two-phase regions in the phase diagram. In order to promote abnormal grain growth in the wires, the authors subjected cyclic heat treatments between 1,200 °C (single phase region) and room temperature (two phase region) for five times under high purity argon atmosphere. In each cycle wires are kept in the furnace for 0.5h and subsequently air cooled. Finally, wires are solution heat treated at 1,300 °C for 30 min and quenched in water. Figure 6 shows wires with bamboo structured grains after the cyclic abnormal grain growth method. Number density of the grain boundaries are diminished, and microstructure contains small number of triple junctions.

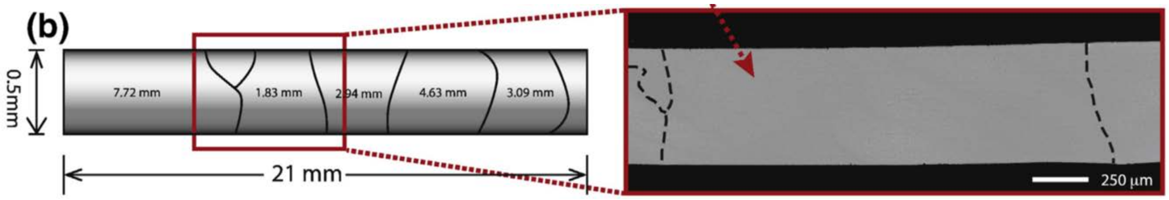

Figure 6. Large-bamboo structured (oligocrystalline) grains that span the cross section of FeMnAlNi SMA wires after thermomechanical processing steps shown in Figure 5.

Electron backscatter diffraction (EBSD) studies show FeMnAlNi wires possess strong [110] texture ([110] refers to the crystal orientation) in the drawing direction as shown in Figure 7.

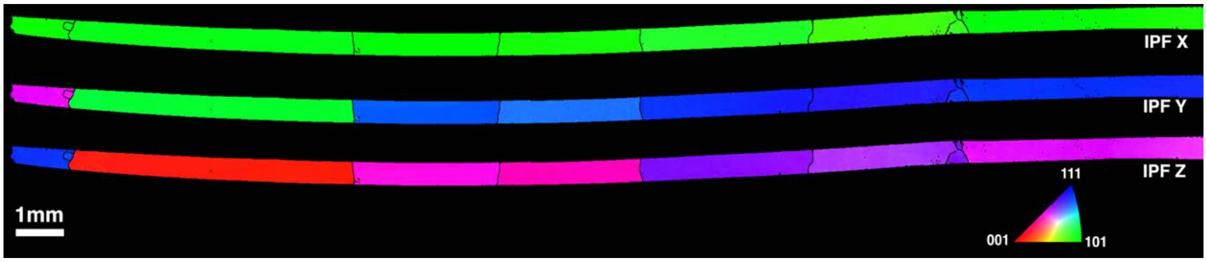

Figure 7. Electron backscatter diffraction orientation mapping of a Fe-34%Mn-15%Al-7.5%Ni (at. %) super-elastic wire aged at 200 °C for 24h after tensile super-elastic test (the super-elastic response is shown in Figure 27c). The colors represent the crystal directions parallel to the drawing direction (IPFX) and the transverse direction (IPFY) and the normal direction (IPFZ), given in the stereographic triangle.

4.2. Apparatus Design to Characterize the Mechanical Response of the Braided Cable

In order to test large diameter cables, current tensile testing grips were redesigned to improve the contact force and prevent slipping during testing. In this section, apparatus design methodologies are explained in detail.

4.2.1. Design and Fabrication of Experimental Setup for Braided Cable Testing:

Wedge grips being used on the wire samples were not able to evenly grip individual strands of the wire in the cables. As a result, slipping was occurred during tensile testing. Therefore, an adaptable grooved grip insert was designed according to the ASTM A1061 "Standard Test Methods for Testing Multi-Wire Steel Pre-stressing Strand."

First Grip Design and Testing: Tensile testing of braided cables requires the grips to withstand large forces. Therefore, S7 A2 tool steel was chosen as a grip material. It is then heat treated at 950°C for 30 minutes to increase the strength. Hardness of the heat-treated grips was measured as 58 Rockwell C. To prevent slipping during testing, grips must be designed with semi-cylindrical grooves as stated in the ASTM standard shown in Figure 8. Therefore, semi-cylindrical grooves were cut on the flat faces of the grip using electron discharge machining (EDM) as shown in Figure 9.

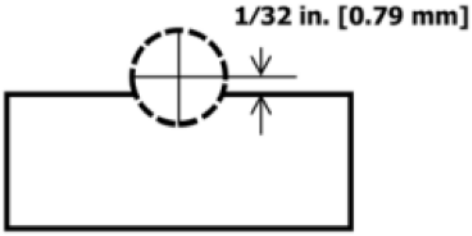

Figure 8. Grip design requirements shown in ASTM A1061 "Standard Test Methods for Testing Multi-Wire Steel Pre-stressing Strand".

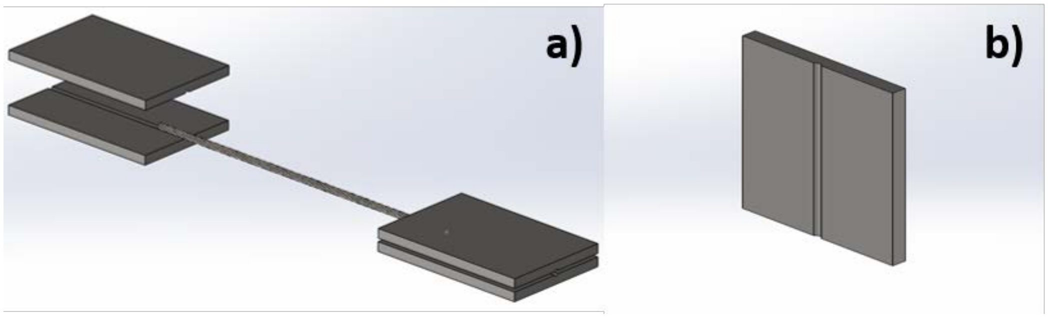

Figure 9. 3D SolidWorks design of semi-cylindrical grooved grip inserts: (a) full assembly with a sample braided cable and (b) an example of a flat face showing a semi-cylindrical grove.

Initial tests were performed on a stainless steel braided 1x7 braid that has been produced using braided cable setup as shown in Figure 10. Each strand has 0.5 mm diameter with a gauge length of 50 mm. Strain measurement has been collected using a laser extensometer with reflective tapes directly attached to the braided cable. An example of braided cable before testing is shown in Figure 10.

Figure 10. Sample braided wire before testing with a gauge section of 50 mm. Two rectangular attachments represent laser tags for strain measurement.

In initial tests, conventional wedge grips with the grooved inserts were used. However, first testing showed slipping between wedge grips and grip inserts, indicating a need for a redesign.

Second Grip Design and Testing: In the second design, grip inserts were made out of tool S7 A2 steel following the same heat treatment as before and hardness of the grip inserts were measured around 60 Rockwell C. Design modifications include a smaller clamp size to fit into clamped grips shown in Figure 11. 6 mm holes were drilled to keep inserts from slipping further. Final built mechanical test setup with grooved grip inserts for measuring monotonic tensile response of the braided cables is shown in Figure 11.

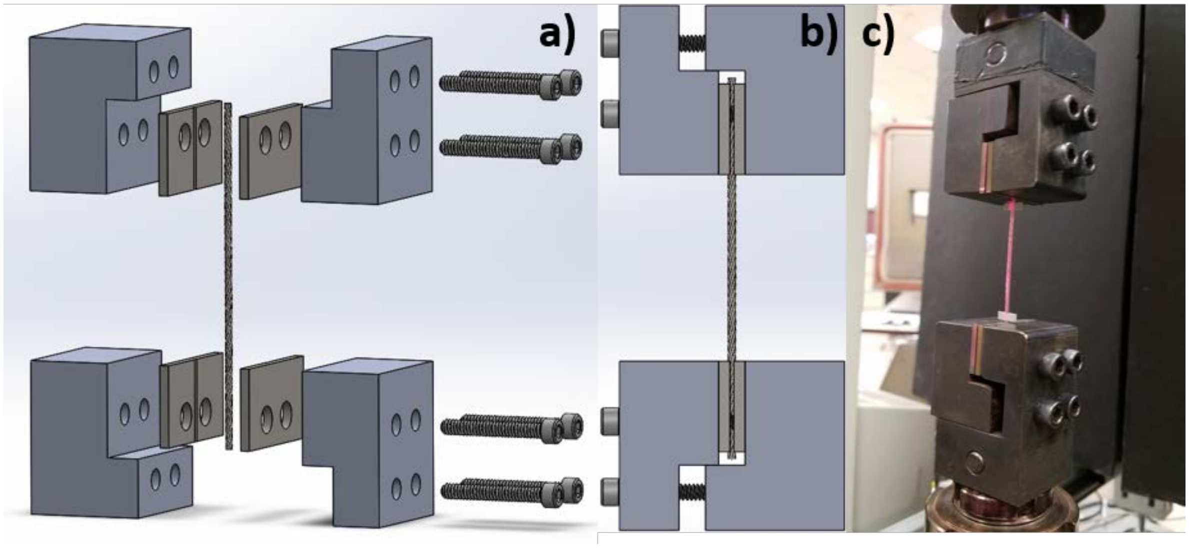

Figure 11. (a) 3D SolidWorks design of mechanical testing grips with grooved inserts for testing cables and (b) Built grips with grooved inserts.

After grip redesign, mechanical characterization of all wires and cables produced in this work were done performed using MTS monotonic screw driven tensile testing machine (MTS is the name of the company). All cyclic tests were performed using a displacement control at a nominal strain rate of 5 x 10^{-4} s^{-1}.

4.3. Designing the Embedding Strategy of Cables in Structural Composites for Crack Detection

The structural mechanics of the concrete-embedded wire system are modeled in Abaqus as an embedded wire in a concrete block. The block is a 50 mm by 50 mm by 150 mm concrete block with a 1 mm radius wire embedded 15 mm from the bottom face of the block. A crack is introduced near the wire to determine the sensing capabilities of the wire near the crack. The model, created for both steel and MSMA wires, applies a load at the center of the block, inducing a crack propagating through the block and wire. As the crack nears the MSMA wire the stress on the wire increases, changing the local martensite volume fraction. The local changes in martensite volume fraction are input into the COMSOL model to simulate external detection by magnetic sensing.

The COMSOL model considers the local magnetic permeabilities of the embedded wire in performing a magneto-static analysis to determine the global magnetic field. With the global magnetic field calculated in COMSOL, a parametric study is then scripted using MATLAB to determine the new magnetic flux near the local phase transformation. The new magnetic field after the MSMA wire locally transforms is recorded and compared to the original magnetic field.

4.3.1. Structural Modeling

A computational model is needed to predict the change in martensite volume fraction in the MSMA wire near a crack under high stress. This model is required to predict the material fracture properties near a crack tip, and the subsequent change in wire phase due to the crack tip field. For proper predictive damage detection and modeling of concrete, crack propagation, SMA phase transformation due to stress, and cohesive bonding between the concrete and wire must be modeled in conjunction with one another. This is achieved by correlating the computational model to experimental testing by recreating experimental testing in the computational framework.

The specimen is subjected to a three-point bend experiment and the model is developed in Abaqus (a commercial finite element software) using extended finite element method (XFEM) to calculate the fracture of the concrete near the crack tip. The computational model is shown in Figure 12.

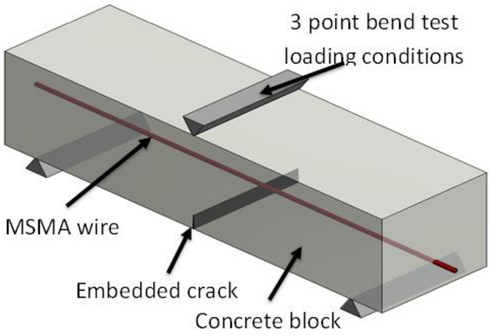

Figure 12. Abaqus utilizes a user material subroutine to calculate the martensite volume fraction of the wire, showing the effect of a nearby crack on the phase of the MSMA wire under an applied load.

The Abaqus model is constructed as a concrete block with an embedded wire using C3D20R elements (a 20-node quadratic brick, reduced integration). The load conditions of a 3-point bend test are applied, with a crack introduced at the bottom of the block to specify the start of the crack propagation. The MSMA wire is modeled using a user material subroutine to calculate the martensite volume fraction as the stresses on the wire change due to the applied load and crack propagation. The crack propagates from the bottom to the top of the concrete block and around the wire, breaking the cohesion between the wire and concrete near the crack. The Abaqus model calculates the stress in each time step, then determines the new martensite volume fraction to input into the next time step.

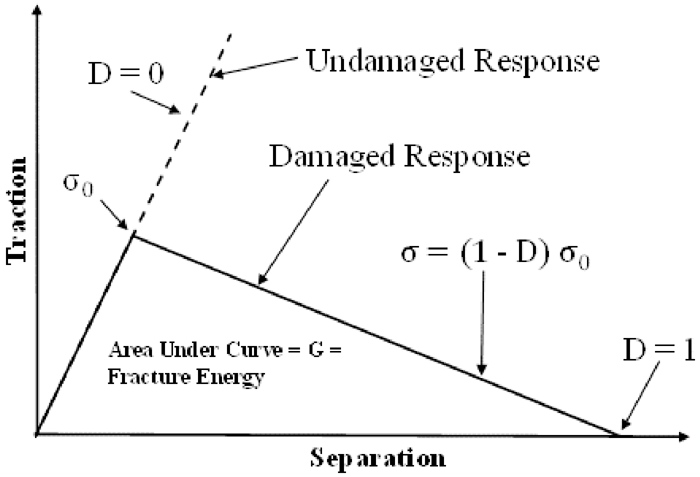

Figure 13. The calculation of damage and fracture uses a cohesive zone model, as shown in this traction-displacement curve. Traction increases until a specified threshold is met, at which point the damage parameter D and fracture energy determine the decrease in traction before complete separation *(23)*.

The concrete's crack propagation utilizes the XFEM in Abaqus. The Abaqus model uses a traction-separation model to calculate the fracture, as shown in Figure 13. This model uses a scalar damage parameter D, which ranges from 0-1 *(23)*. This model requires the fracture energy of the material, which is derived from literature and experimental testing.

4.3.2. Structural Modeling Validation

Experimental testing was conducted on the concrete block and wire system in the manner previously described. The displacement-controlled testing showed a close relation between experimental testing and computational modeling to the point of fracture, crack propagation, and loading on the MSMA to induce phase transformation. The experimental and computational results are shown below in Figure 14.

The Abaqus model utilizes a User Material Subroutine (UMAT) to characterize the shape memory alloy behavior present in the wire. The foundation and background for the constitutive model for the SMA structural response is provided elsewhere *(24)* and has been used to analyze a number of SMA applications *(25, 26)*.

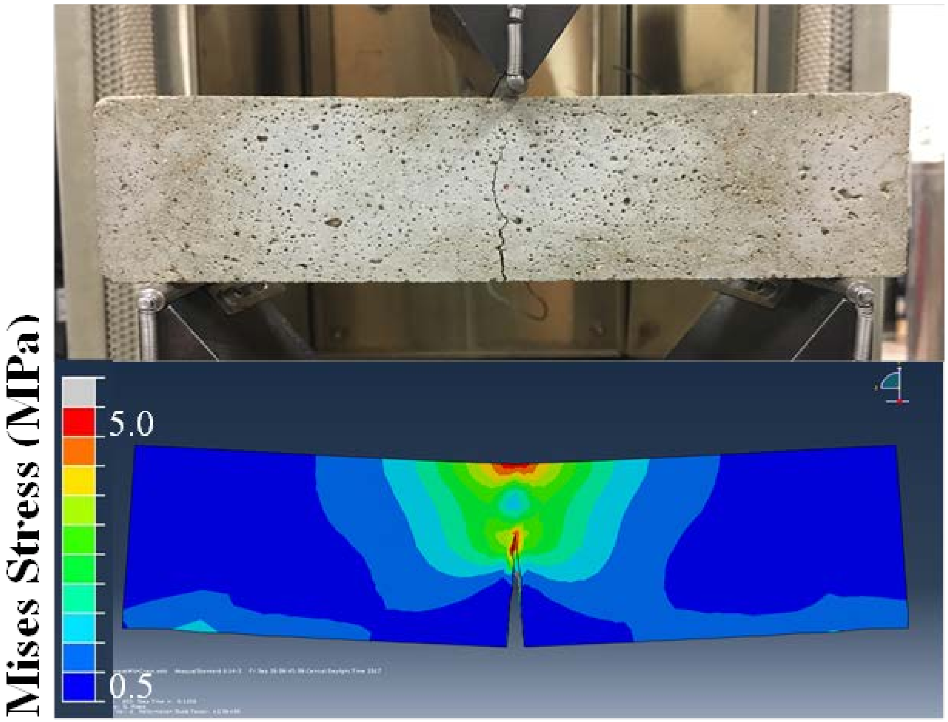

Figure 14. The 3-point bend test was performed in both the experimental and computational domains.

4.3.3. Magneto-Static Modeling

To model the changes in the magnetic response of the SMA wire and its detection, it is necessary to create a computational model to simulate the SMA wire's magnetic response to an internal crack and its effect on a magnetic field. To create this model, the framework was built in COMSOL Multiphysics (a cross-platform finite element software to solve coupled systems of partial differential equations) to model the magnetic field for a variety of geometries as a small portion of the wire, near a stress concentration (near the crack tip), undergoes a phase transformation. This model is adaptable to variable geometries and phase transformations to correlate experimental and computational results. The geometry used in this model matches the structural model and experimental testing geometries while introducing a magnetic field and sensor to simulate detection capabilities. A magnet is located on one side of the sample, while the field is measured on the opposite side using a point sensor as shown in Figure 15. Calculating the change in the magnetic field as a section of SMA wire undergoes a phase transformation allows sensing data to be correlated with wire transformation. When the model is calibrated to correlate well with the experimental results, it serves as a method to locate and detect cracks and stress concentrations inside the concrete.

COMSOL magneto-statics utilizes Ampere's Law and Gauss's Law with the assumption of zero applied currents.

$$\nabla \cdot B = -\nabla \cdot (\mu \nabla \emptyset_m - \mu M) = 0 \qquad [1]$$

where:
B = Magnetic flux density,

μ = material magnetic permeability, and
M = magnetization field.

The magnetic permeability is defined as:

$$\mu = \mu_0 \, \mu_m \qquad [2]$$

where:
μ_0 = the permeability of free space, and
μ_m= the material relative permeability.

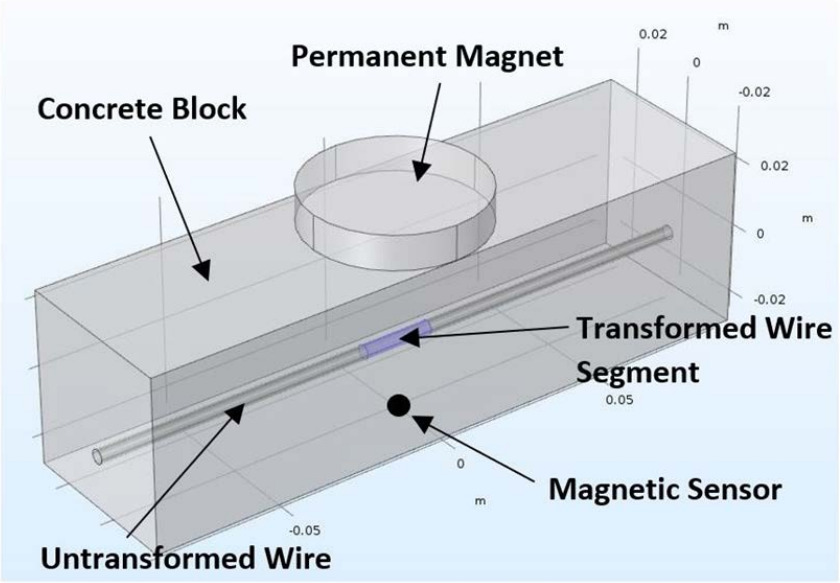

Figure 15. The COMSOL model consists of a wire with a transformed portion at the center of the concrete block, with a magnet on one side of the block and probe on the opposite side.

The computational model is parameterized to allow for scripting and design optimization. The magnetic field normal flux is computationally calculated for a magnet with known parameters with the probe moving axially away from the magnet. These results are then compared to experimental results for the same parameters and a known analytical solution for this simple geometry to ensure the parameters, computational model, and scripting interface are accurate. The COMSOL model, analytical solution, and experimental results are all shown in Figure 16.

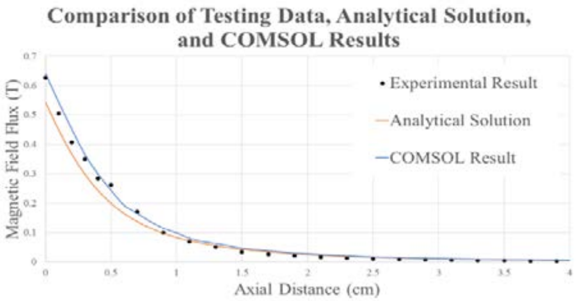

Figure 16. For a simple, known geometry the COMSOL computational model matched very closely to both experimental and analytical results.

4.3.4. Form Factors

A variety of form factors are available for the wire, with the overall wire shapes limited to single wires and braided cables. The wire radius, number of wires, and wire location are all adjustable parameters in the model. The single wire model shown in Figure 16 is partitioned along the length of the wire into axisymmetric segments, each with a controllable magnetic permeability and size. As mentioned previously, the local magnetic permeabilities of the wire are inputs using the known magnetic permeability of each martensite volume fraction calculated by the Abaqus structural model.

The braided wires modeled in COMSOL are constructed using a single wire at the center and 6 wires twisted around the center wire in a helical pattern. The radius of the wires shown is 1 mm, leading to a cross-sectional area in the braided cable 7 times that of the single, small wire. To compare the effectiveness of the braided cable and the single wire, a second single wire model is created with the same cross-sectional area as the braided cable. The magnetic flux through the wire varies depending on the wire geometry and whether the wire is braided or not, as can be seen in the cross-section in Figure 16, where the magnetic flux follows the braided wires. In a single, large wire the flux remains fairly constant across the cross-section, but the braided cable shows a more consistent flux along the length of each individual wire, tangential to the cross-section. For the braided configuration, a change in magnetic permeability would affect the magnetic flux down the wire in addition to near the local phase transformation.

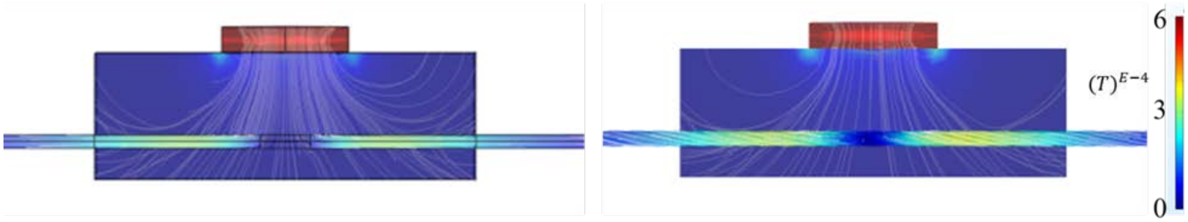

Figure 16. A large wire (left) and braided cable (right) of the same cross-sectional area are created to compare a cable configuration. The cable consists of 6 wires braided around a straight wire of the same size. While the single wire has a consistent magnetic flux across the cross-section, the braided cable shows a more consistent flux along the individual wires.

COMSOL allows for MATLAB scripting, which is utilized to compare the magnetic flux along transformed and untransformed local regions in the MSMA wire. The search for internal phase transformations, and thus internal cracks, is simulated by moving the sensor and magnet along the length of the concrete block, centered on the MSMA wire. The wire has a single region of phase transformation at its center, with the rest of the wire untransformed as shown in Figure 17. The magnetic flux is recorded, with the results compared to the untransformed portion of the wire.

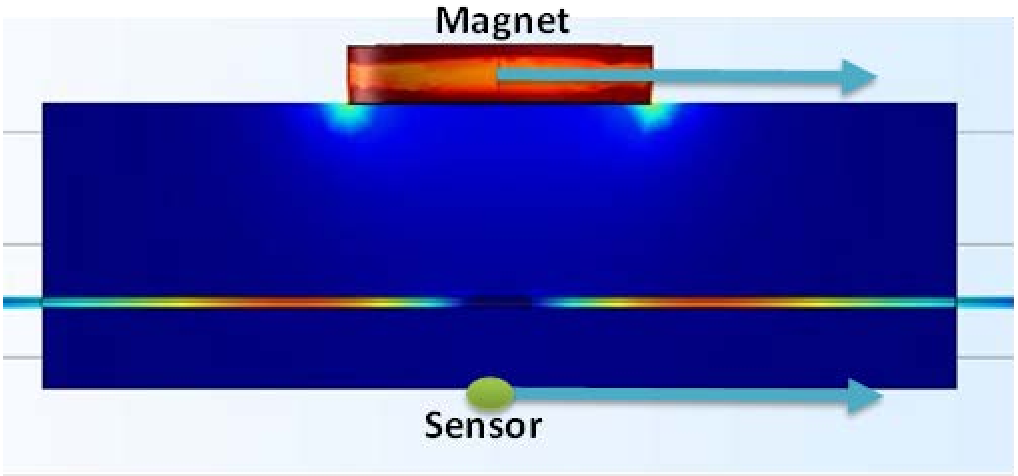

Figure 17. The sensor and magnet move along the length of the concrete block measuring the external magnetic flux in the vicinity of an internal crack.

5. FINDINGS

5.1. Setup Design and Cable Fabrication

5.1.1. Design and Fabrication of Wire Braiding Test-Setup

Cable design requires different braiding configurations. In order to test various cable designs, an equipment that is capable of fabricating different braid configurations is required. Therefore, small laboratory scale wire braiding cable was designed. Fort Wayne Metals Company is an expert on wire fabrication braiding for 70 years. An onsite visit to Fort Wayne Metals was scheduled in order to gain insights on wire braiding process. The 3D SolidWorks design of the laboratory scale cable setup is shown in Figure 18.

Laboratory scale wire braiding setup can be divided into two parts; mechanical design, electronics/control design.

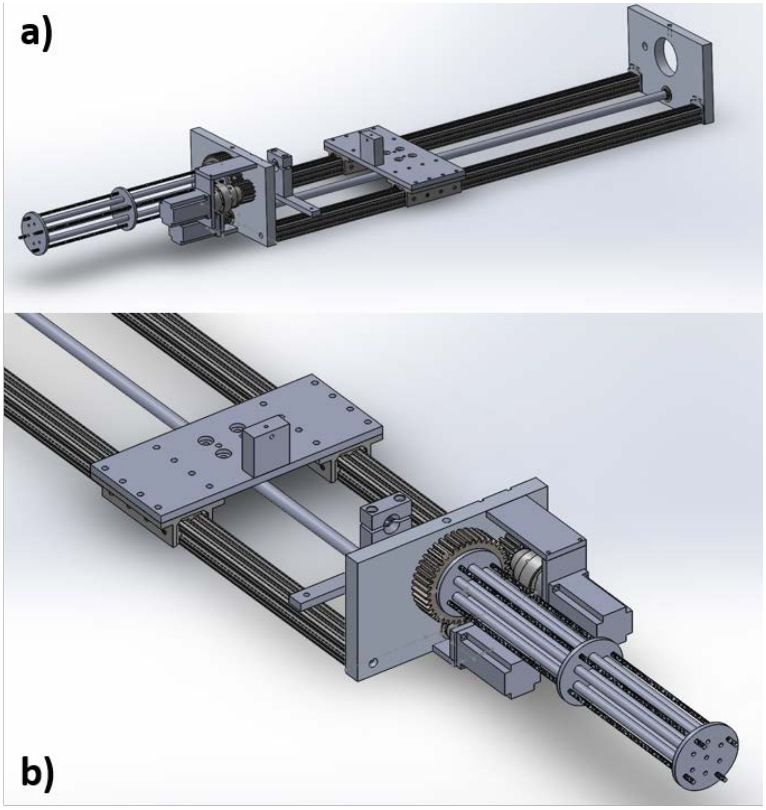

Figure 18. The 3D SolidWorks design of the laboratory scale wire braiding test setup shown in two different views.

Mechanical Parts Design of Wire Braiding Setup: Wire braiding test setup is composed of three main parts: rotating wire feeder, adjustable winder, and sliding cable collector.

Rotating Wire Feeder: Rotating wire feeder is composed of seven cones that guide the wires to die. All wires are manually fed to the cones where each cone has its own wire tension mechanism that is attached to the cone ends. This tension mechanism prevents entanglement of wires during shaft rotation. Design and fabricated rotation wire feeder part are shown in Figure 19.

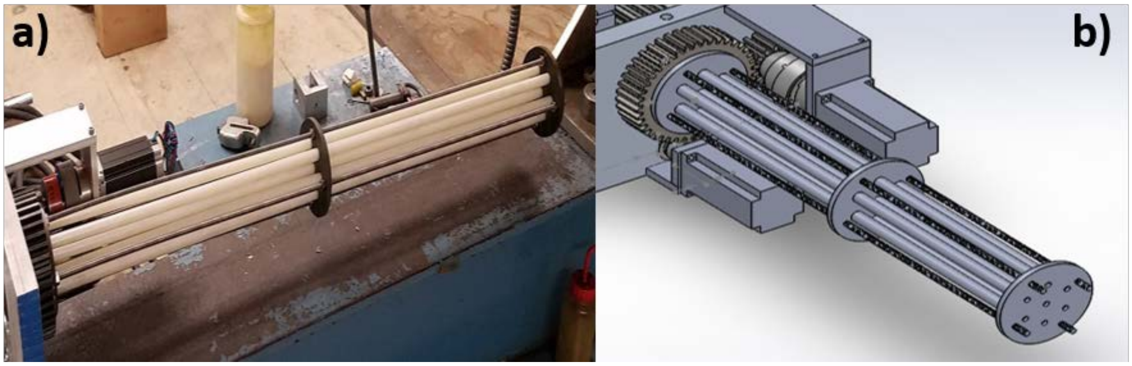

Figure 19. Rotating wire feeder part of the wire braiding test setup (a) built and (b) preliminary 3D SolidWorks model.

Adjustable Winder: Adjustable winder is the middle part of the wire braiding setup where all wires are fed through seven individual holes (Figure 20). It is composed of two different size hardened tool steel gears where small gear is attached to a motor driver. In the current design, large sized gear has seven holes and this allows to produce commercial 1x7 patterned cables. However, gear is adjustable; hole diameter or number of holes in the gear can be changed and different cable configurations can be fabricated.

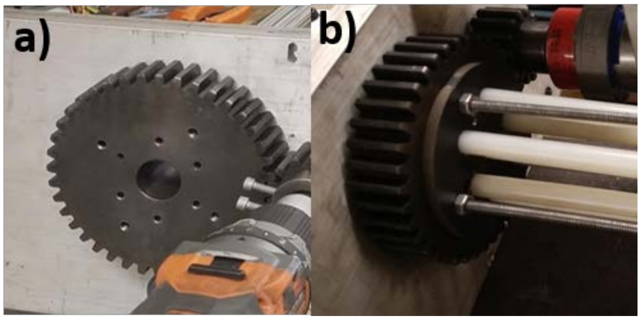

Figure 20. Adjustable winder part of the laboratory sized wire braiding test setup shown in two different views.

Sliding Cable Collector: Sliding cable collector part (Figure 21) composed of two separate dies attached to a long screw. One of the dies has a hole where all wires are collected, and the other die ensures that the cable has a tension as the cables are fed through. These two dies move backwards and collect the cables as motor operates and rotates the shaft.

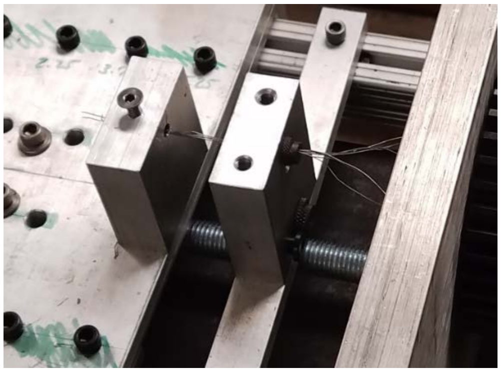

Figure 21. Sliding cable collector part of the wire braiding test setup.

Electronic/Controls Design of Wire Braiding Setup: Electronic controls of the setup include two L298 motor drivers, two 27 bipolar stepper motors, an Arduino mega, and two 5 Volt power supplies rated for 3 amps each. Complete electronic circuit that runs the setup is shown in Figure 22.

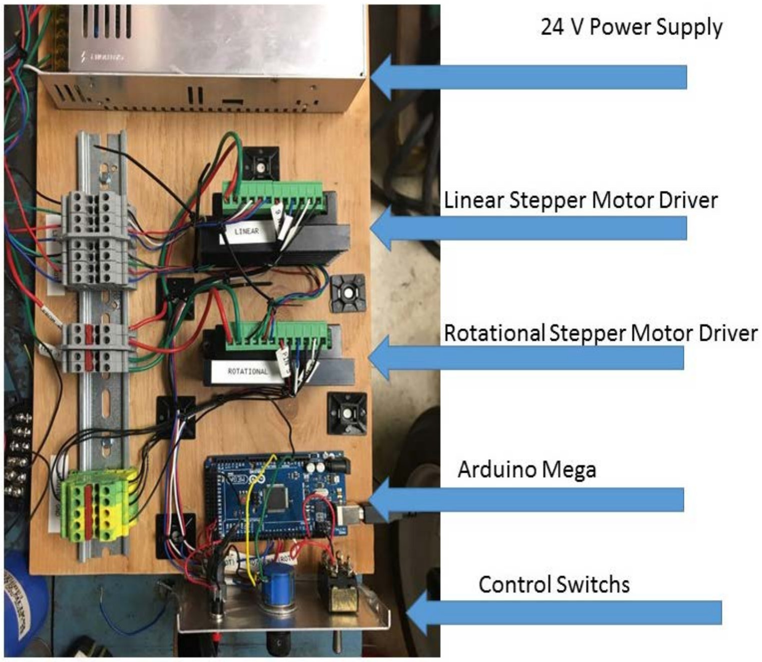

Figure 22. Complete electronic circuit of the wire braiding test setup. Power supplies, stepper motor drivers, Arduino mega and control switches are indicated as blue arrows.

An Arduino script is developed that allows both motors to drive at a different speed. Control unit includes an interrupt pin to prevent timing difference between the two stepper motors and switches. In order to inhibit torque deficiency, a single 24-volt power supply is used to power everything instead of two separate 5-volt power supplies. In addition, heavier duty stepper motor drivers replaced the small L298 motor drivers.

Final experimental laboratory scale cable braiding setup is shown in Figure 23.

Figure 23. Finished experimental setup for fabricating braided cables.

5.1.2. Fabrication of Fe-SMA Braided Cables

An example of a fabricated braided cable (1x7 configuration) using the wire braiding setup is shown in Figure 24.

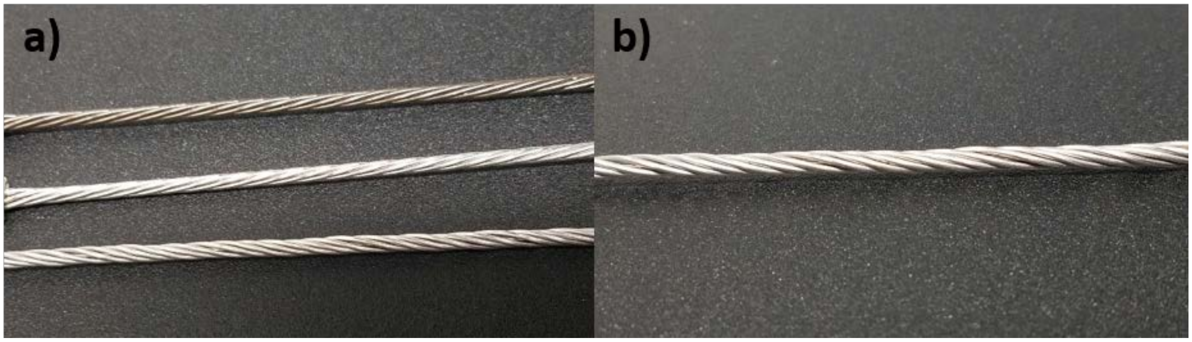

Figure 24. (a) Three different braided cables made using the braiding setup and (b) close-up of a single braided cable.

5.1.3. Design and Fabrication of Atmosphere-Controlled Quartz Furnace

FeMnAlNi wire with coarse grains shows 6.7% recoverable strain levels while maintaining its high strength when it is aged at 200 ºC 24h (as shown in Figure 27c). For SHM applications, other forms of components (cables, large dimension rods, etc.) are required. Cables are advantageous due to their distributed interface with surrounding matrix and their locally uniaxial stress levels. In addition, when the SHM applications considered, cables and wires with long lengths are required. Therefore, a custom-made furnace with a capability of heat-treating individual wires longer than 200 mm is designed. Preliminary SolidWorks design of the custom-made furnace is shown in Figure 25.

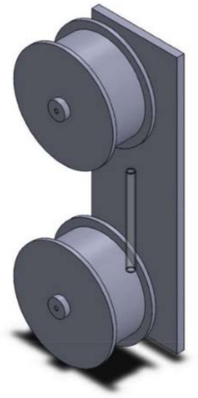

Figure 25. Design of atmosphere-controlled furnace with rollers capable to heat treat longer wires.

Heat treatment of Fe-SMAs require inert atmosphere, therefore the furnace is atmosphere controlled with high purity argon. Wires from the top spool will be fed through a quartz tube and heat-treated wires will be picked by the bottom spool. Each spool will be attached to a motor and wire speed will be adjusted to different heat treatment durations. After heat treatments are completed, wires will be air cooled. By repeating this process, cyclic heat treatments will be performed on individual wires.

5.2. Mechanical Property Characterization

5.2.1. Method to Control Superelastic Stress Levels by Nano-Precipitation

In addition to large grains, nano-sized precipitates are another necessary condition to obtain super-elasticity in FeMnAlNi alloys. Figure 26 shows 4-6nm and 6-9nm sized B2 nano-precipitates when the alloy is aged at 200 °C for 1h and 3h respectively.

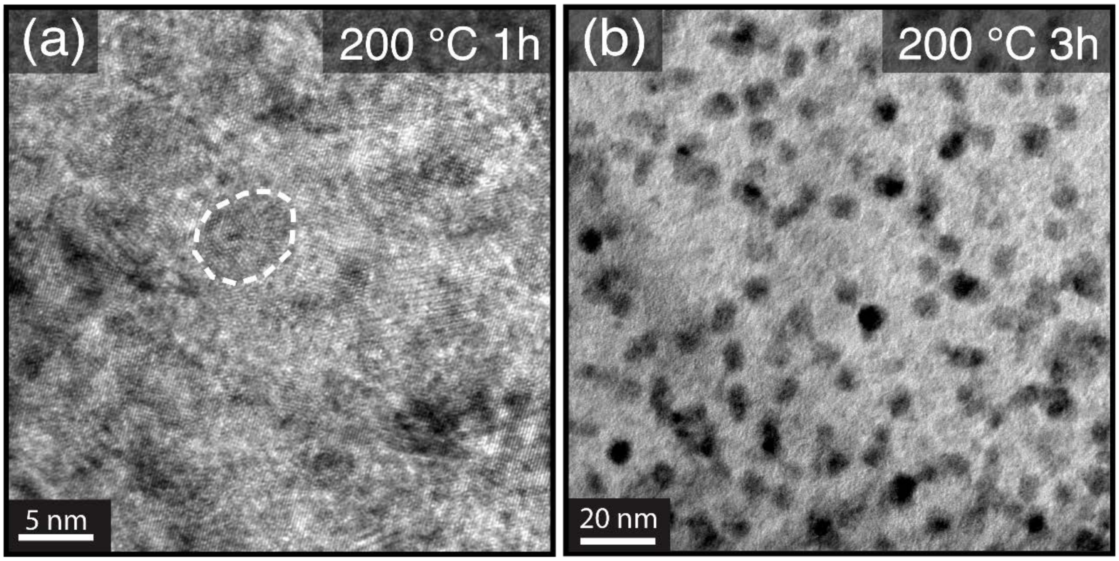

Figure 26. Microstructure of the Fe-34%Mn-15%Al-7.5%Ni (at. %) alloy; (a) high resolution TEM image showing B2 precipitates after aging at 200 °C for 1h. Dashed white line represents one of the B2 precipitates. (b) Conventional TEM image of B2 precipitates after aging at 200 °C for 3h. Dark regions represent B2 nano-precipitates.

The size of the nano-precipitates increases as the duration of aging time increases. The volume fraction and size of the precipitates greatly influence the super-elastic characteristics such as transformation stress levels, transformation temperatures, martensite morphology and hysteresis.

Effect of nano-precipitates on the super-elastic behavior can be clearly seen in Figure 27. The authors have performed uniaxial tests on coarse grained wires with different nano-precipitate sizes. The authors deformed the specimens at a nominal strain rate of 5×10^{-4} s^{-1} and increased applied strain levels 1 % increments until failure. Figure 27a-c shows the stress-strain response of Fe-34%Mn-15%Al-7.5%Ni wires at room temperature after aging at 200 °C (a) 1h, (b) 3h and (c) 24h. Summary of the critical transformation stress levels of FeMnAlNi wires aged at different durations can be seen Figure 27d.

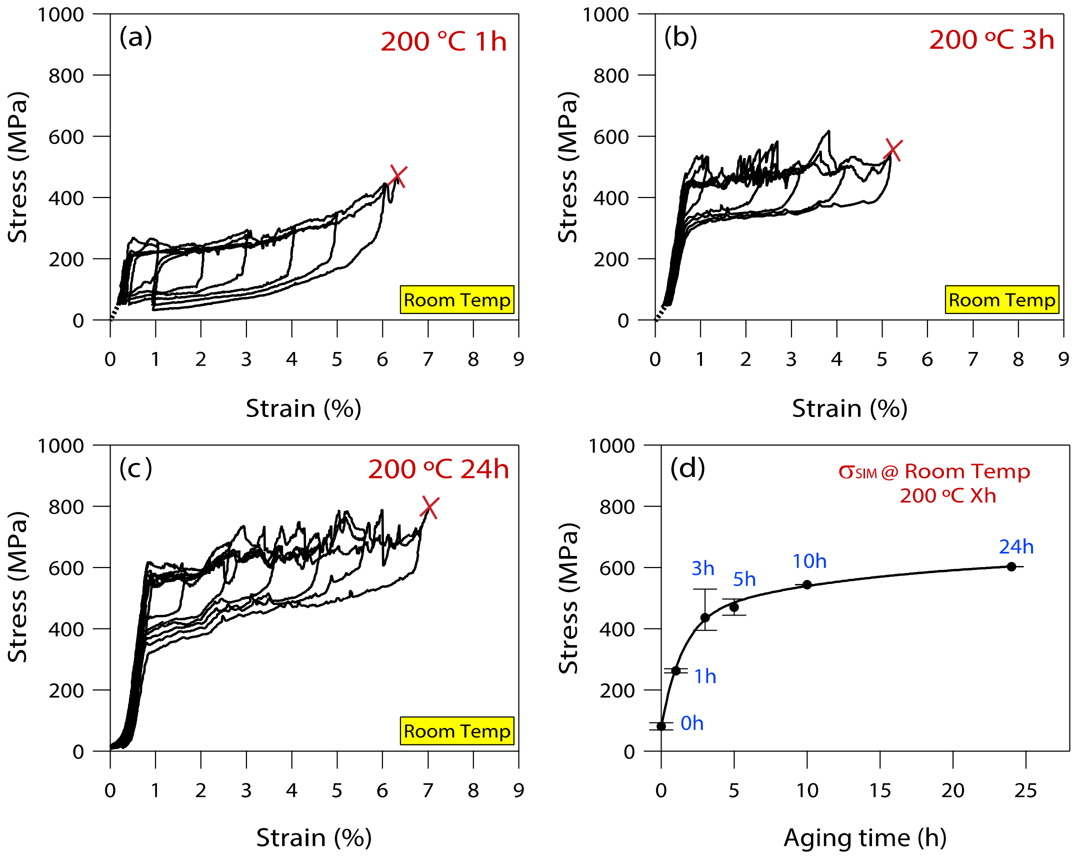

Figure 27. Room temperature tensile super-elastic responses of Fe-34%Mn-15%Al-7.5%Mn (at.%) wire subjected to the cyclic abnormal grain growth method, followed by solution heat treatment at 1300 °C, and aging at 200 °C for (a) 1h (b) 3h and (c) 24h, and (d) Summary of the critical stress for stress induced martensitic transformation versus aging time of the Fe-34%Mn-15%Al-7.5%Ni wires after cyclic abnormal grain growth and aging at 200 °C.

As shown in Figure 28, stress levels increase for short aging duration and then plateauing around 600 MPa for aging treatments longer than 5h. This happens due to a decrease in transformation temperatures which again depend on the size of the precipitates and composition change in the matrix due to nano-precipitates.

In all aging conditions, average transformation strain levels are about 7% and strain level at fracture does not change notably. When the wires are aged at 200 °C for 24 hours, it is shown that FeMnAlNi wires can transform and recover up to 6.7% strain with a critical stress level of 600 MPa. This strength level with low hysteresis has not been previously reported in polycrystalline FeMnAlNi wires or sheets.

5.2.2. Characterization of Mechanical and Super-elastic Properties of Cables

Stainless steel and NiTi braided cables that have been sent by our collaborator company Fort Wayne Metals have been tested using this new design. With this new design, grips were able to withstand large amount of stress levels and sustain large amount of deformation up to 50% as shown in stainless steel cable tensile test in Figure 28. To characterize full mechanical behavior of a common stainless-steel braided cables, cyclic tests with 1% stain increment was performed up to 8% strain, and then it was loaded until failure.

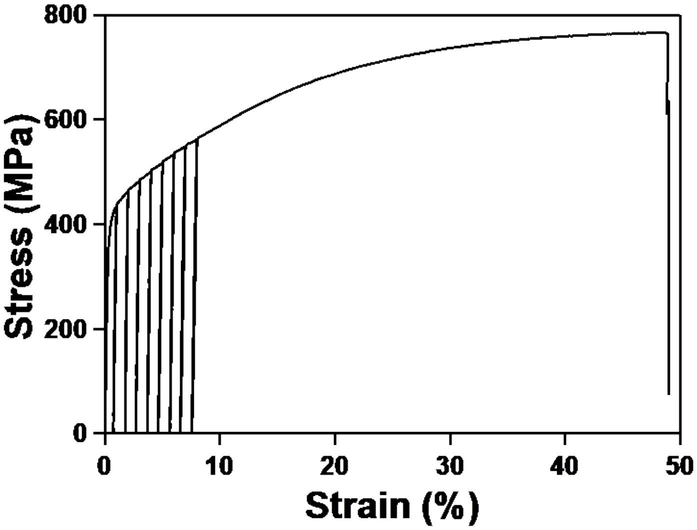

Figure 28. Stress strain behavior of a stainless-steel cable.

It is seen from Figure 28 that stainless steel cable yield strength is around 410 MPa; however, it does not recover applied deformation after load is removed. The authors have also tested super-elastic NiTi braided cable using the new grooved grip inserts. Similar to stainless steel cable, incremental cyclic tests were performed until full transformation is complete. Super-elastic NiTi braided cable mechanical behavior is shown in Figure 29. Critical transformation stress level of super-elastic NiTi cable at room temperature is around 520 MPa and it can fully recover deformation up to 8%.

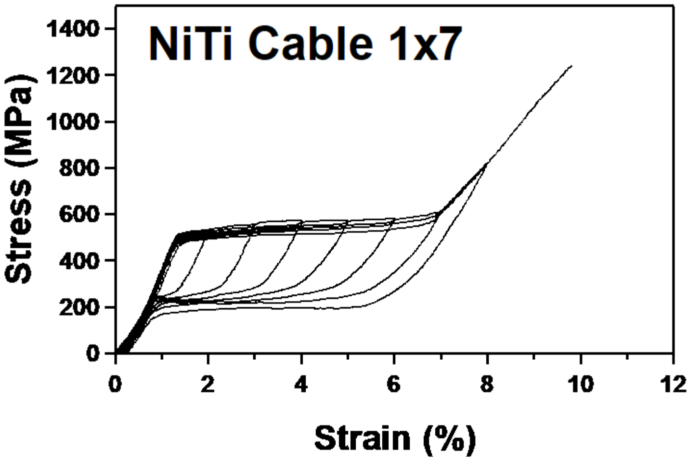

Figure 29. Stress strain behavior of NiTi SMA cable showing 7% recoverable deformation.

5.3. Magneto-Mechanical Property Characterization

5.3.1. Design and Fabrication of an Experimental Setup for Magnetic Response

Test Stand: In order to measure the change in magnetic behavior of the braided cables and validate simulation efforts, the authors developed wire testing grips and an attachment for measuring magnetic changes in the braided cables (as shown in Figure 30). In magnetic measurements, choice of material of the setup is important, since it can influence the final measurement. In this case, the authors have chosen a nonmagnetic material aluminum for the wire grips. Since non-magnetic aluminum is not going to be magnetized during testing, its effect on the final measured magnetization of the braided cable is eliminated. For holding magnetic sensors and biasing magnet, the authors have developed an attachment that can be directly placed to the aluminum grips using screws. The attachment contains four rails that can hold the magnetic hall sensor and a biasing magnet at different configurations. The rails allow the sensor and magnet to change their distance horizontally from the wire/cable being tested. The attachment also has a capability to move vertically. All components of the attachment were 3D printed using PLA and preliminary magnetic measurements were collected.

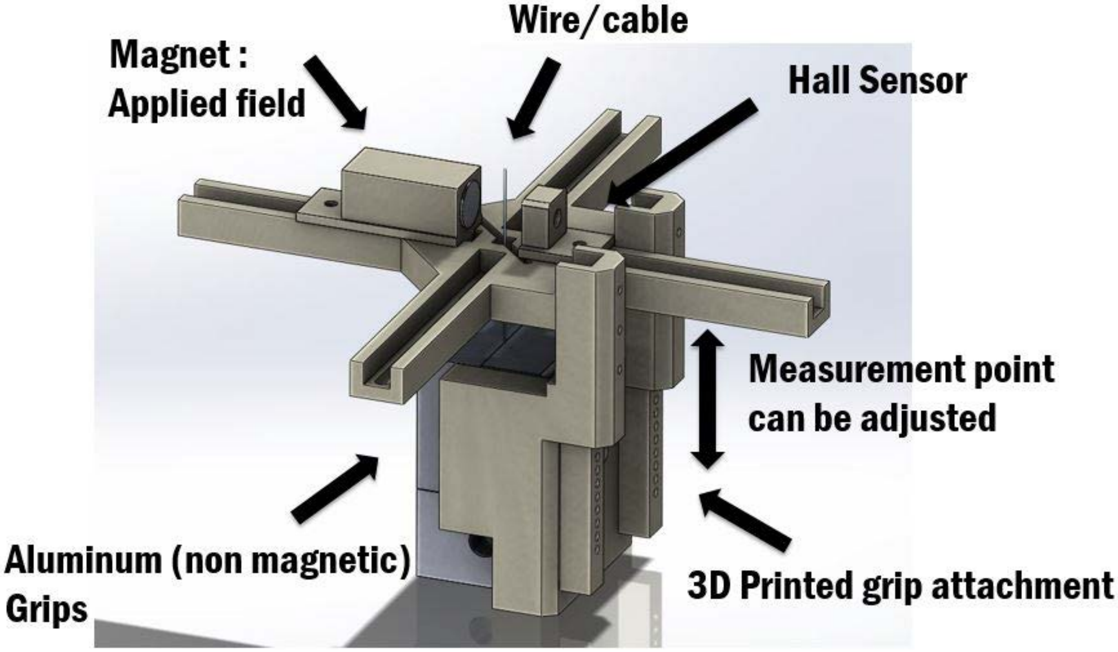

Figure 30. Full magnetic test stand and assembly.

Hall Sensor: All experiments were performed using a Lakeshore Cryogenics HGT-3010 hall sensor. The sensor was delivered along with calibration data provided by Lakeshore. This calibration data was loaded on the hall sensor's cable before being used for testing. The sensor was used in conjunction with a Lakeshore model 460 3 channel gauss meter.

Magnet: The requirement for the magnet is to be able to saturate the material's parent austenite phase. As shown in Figure 31, saturation magnetization for the parent phase was measured as 0.5 T. The magnet type was chosen as ½-inch diameter 2 inch long NdFeB grade 42 permanent magnet. The maximum field measured at the surface was 0.63 T, which is adequate for saturating the parent phase.

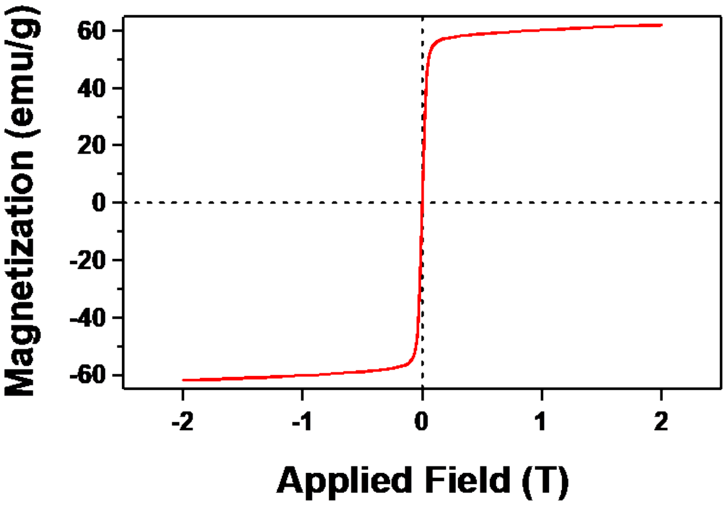

Figure 31. Relationship between magnetic flux density (B) and field strength (H) of an austenitic FeMnAlNi wire aged at 200 °C for 3h.

Data Processing, Filter Design: Due to the sensitivity of the hall sensor and magnetic setup, significant amount of noise was affecting the signal quality. Figure 33 is a completely unprocessed signal collected from a steel wire test. By placing unprocessed data into the frequency domain, noise was evaluated and countermeasures were created with digital filter in LabView.

Data Processing, MATLAB Script: Once the data was collected and filtered, it was placed in a MATLAB script that applied a smoother to the magnetic data. After it was smoothed, the data was adjusted such that magnetic data had the same number of readings as the stress and strain data from MTS tension setup. The result of this is that the magnetic data is smoothed, and able to be compared easily with the stress and strain data from the experiments.

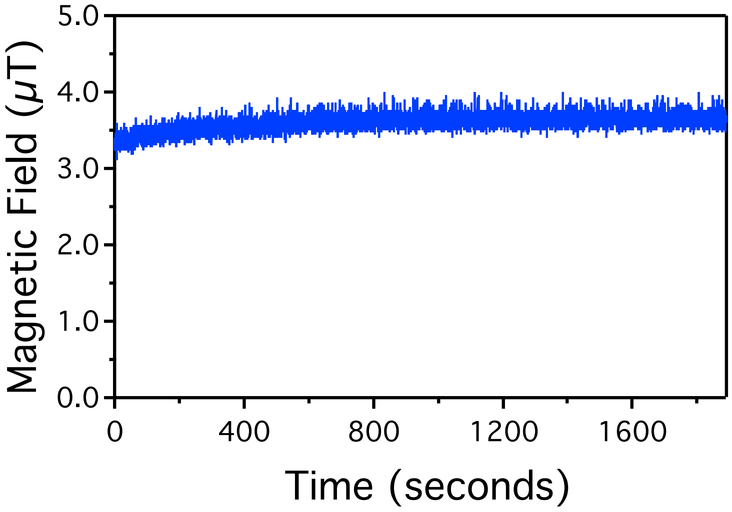

Figure 32. Unprocessed time domain response of a stainless-steel cable subjected to incremental strain test.

Sensor Distance Compensation: It is known that magnetic field of a sensor decays exponentially with increasing distance. In order to find the correct location where magnet can provide sufficient field to saturate the sample, it is important to characterize the magnetic field decay with respect to distance. Figure 33 represents the magnetic field of the sensor plotted as a function of distance from the sensor.

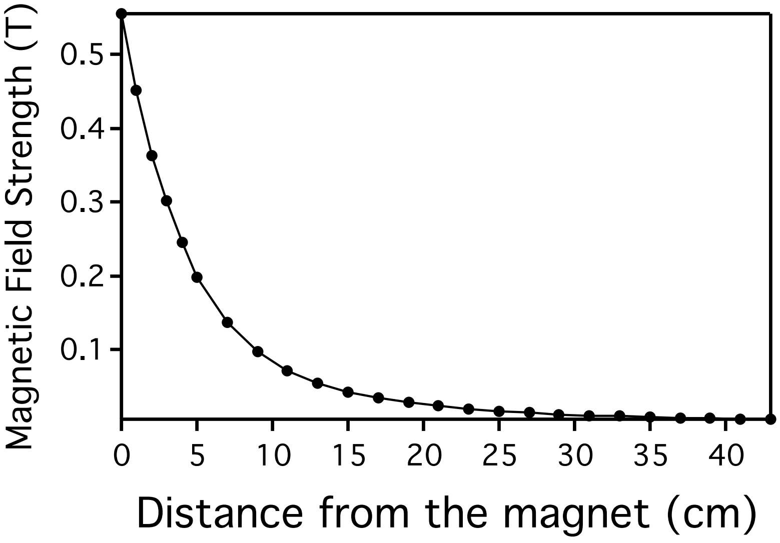

Figure 33. Measured magnetic field decay as a function of distance from the magnet surface.

As shown in Figure 33, magnetic field strength quickly decays to 0.1T at a distance 1 cm from the magnet. This implies that, minor errors in placement of the sample will result in large errors in the saturation field. The error can be minimized by placing a stronger magnet where minor changes in the distance would not create a field decay of 0.5T.

5.3.2. Magneto-Mechanical Response of Wires and Braided Cables

Magnetic Properties of Austenite Phase: FeMnAlNi SMA shows spontaneous magnetization change on loading and unloading. To measure FeMnAlNi saturation magnetization in a fully austenitic state, a wire having a 0.5 mm diameter was solution heat treated at 1,200 ºC for 30 minutes and quenched in water. Afterwards, ratio of wire's magnetic flux density to field strength (B/H) was measured using a superconducting quantum interference device (SQUID). Figure 31 shows the B-H curve of a FeMnAlNi super-elastic wire in austenitic state aged at 200 °C for 3h. According to Figure 31, an applied field of 0.5T is enough to fully saturate austenite phase. Magnetic hysteresis is around 2.3mT (which is small) and saturation magnetization of austenite phase is 60 emu/g.

Magnetic Properties of Martensite Phase: At room temperature FeMnAlNi alloys are in an austenitic state. In order to achieve a martensitic structure at room temperature, martensite phase needs to be stabilized by deforming a small grain sized microstructure. In order to generate small grain size, FeMnAlNi wire was solution heat treated at 1,200 °C for 30 minutes and aged at 200 °C for 30 minutes. After solution and aging heat treatment, FeMnAlNi wires were deformed in order to induce martensitic structure. Microstructure of the sample were examined after loading, using optical microscopy to ensure that it is fully martensitic. Similar to austenite, B/H curve measurements were conducted on the martensite shown in Figure 34.

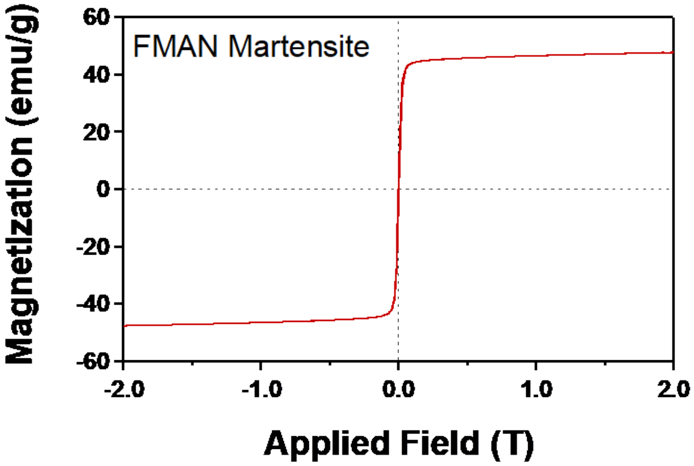

Figure 34. Relationship between magnetic flux density (B) and field strength (H) of an austenitic FeMnAlNi wire aged at 200 °C for 3h.

5.4. Magneto-Mechanical Finite Element Modeling

This section discusses the results found by using the previously mentioned methods for structural and magnetic evaluation. First, the structural results will calculate the change in martensite volume fraction and necessary stress fields from the embedded crack and MSMA wire system under an applied load. The change in martensite volume fraction is then input into the COMSOL magneto-static model to calculate the change in an external, measured magnetic field. This magnetic flux profile is then used to determine the presence and location of internal cracks near the wire.

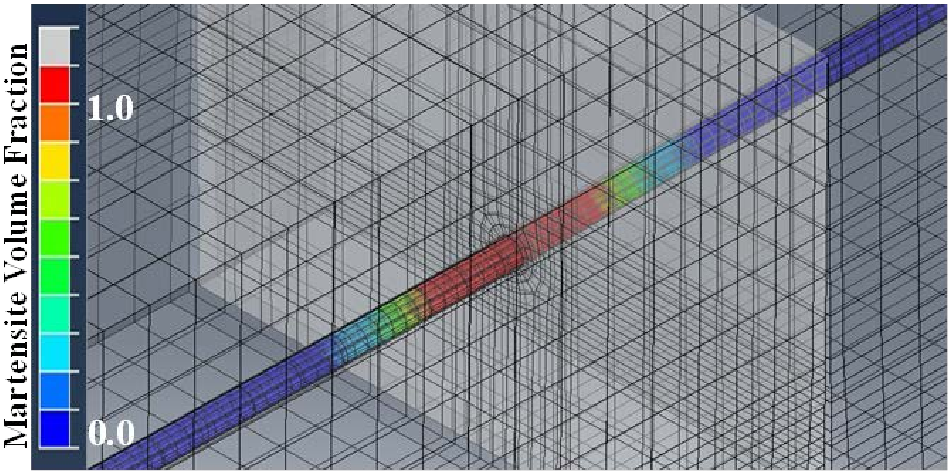

Figure 35. Near the crack the wire fully transforms from austenite to martensite.

5.4.1. Structural Results

The computational modeling of detecting an embedded crack begins with the change in martensite volume fraction of the MSMA wire near the crack. As the load is applied to the concrete, the stress in the near crack tip field transforms the MSMA wire in the locations nearest the crack. The Abaqus model predicts a phase transformation length of approximately 1.5 cm in the MSMA wire nearest the crack, as shown in Figure 35.

The model also demonstrates a major increase in loading on the wire near the crack before the crack has reached the wire. While the stresses far away from the wire demonstrate a normal crack tip field distribution, the loads near the wire are redistributed along the wire length, increasing the stress in the MSMA wire near the crack as shown in Figure 36.

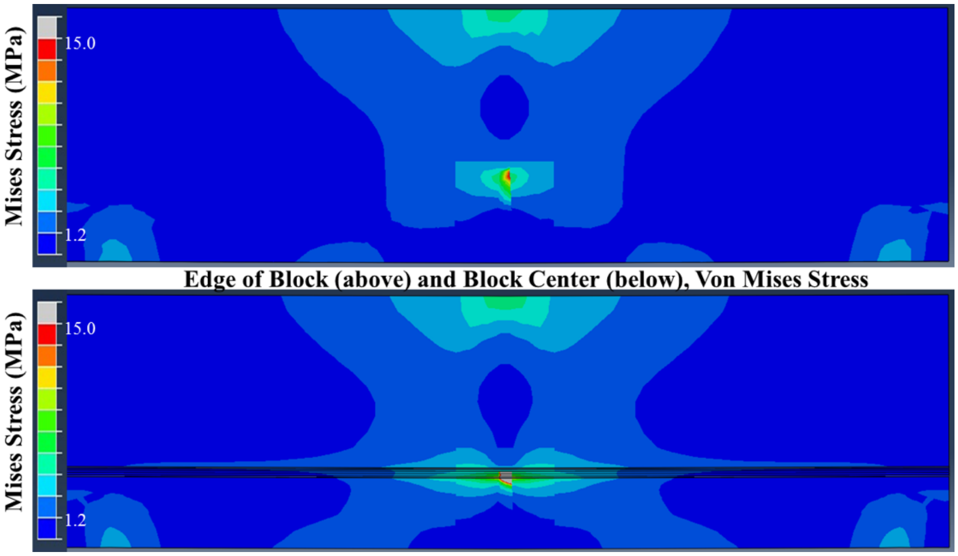

Figure 36. The stress field away from the crack (top) shows a normal crack field, while the field near the wire (below) demonstrates the increases stress along the wire near the crack, causing the phase transformation.

5.4.2. Magnetic Sensing Results

With the change in martensite volume fraction determined from the structural computational results for a nearby embedded crack, the magneto-static model inputs the MSMA wire with a 1.5 cm transformed length of wire at its center. A magnet and sensor are moved down the length of the wire on each side of the concrete block to measure the change in magnetic flux near the crack. These scripted search results are shown in Figure 37. With the sensor located across from the center of the magnet, the maximum change in magnetic flux occurred when the crack was in line with the edge of the magnet, with a symmetric response as the other edge of the magnet passed by.

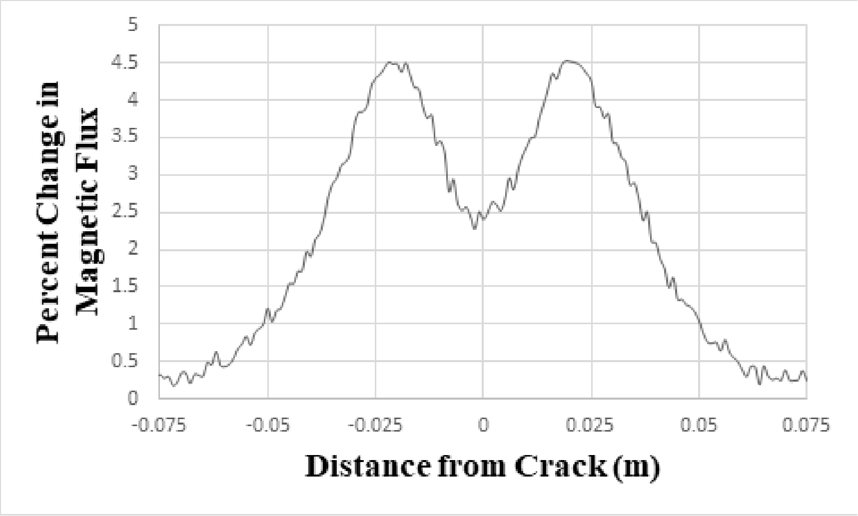

Figure 37. The change in magnetic flux measured increases as the sensor passes by the local wire transformation shows a distinct pattern, with an increase in magnetic flux of over 4 percent. The distinctive dip in the center of the field signifies the location of the internal crack.

Since the maximum change in magnetic flux occurred near the edge of the magnet, a new search for cracks was performed with the sensor now located across from the edge of the magnet as shown in Figure 38. This resulted in larger change in magnetic flux as shown in Figure 39 due to the larger magnetic flux on the edge of the magnet as opposed to at its center.

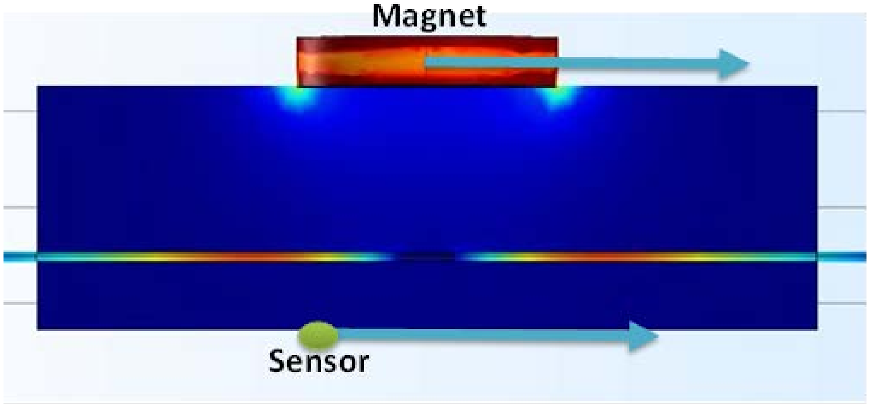

Figure 38. Moving the sensor opposite the edge of the magnet nearly doubles the detected change in magnetic field. The point where the percent change goes from positive to negative signifies the location of the internal crack.

The braided cables show a similar result when detecting a phase transformation, but with a much larger change in magnitude due to the increase in the cable's cross-sectional area. Comparing the braided wire to a single wire with the same cross-sectional area, the braided cable shows a very similar recorded magnetic flux compared to the single wire, as shown in Figure 39. Additionally, the increase in magnetic flux presents a slightly more distinct profile over a slightly smaller area for the braided cable when compared to the single wire. When accounting for the cross-sectional area of the cable and wire, the effect of an identical phase transformation yields very similar magnetic sensing results for both a single wire and a braided cable. The larger change in magnetic flux in both of these tests as compared to the 1 mm radius single wire model highlights the correlation between wire radius and magnetic sensitivity of the system.

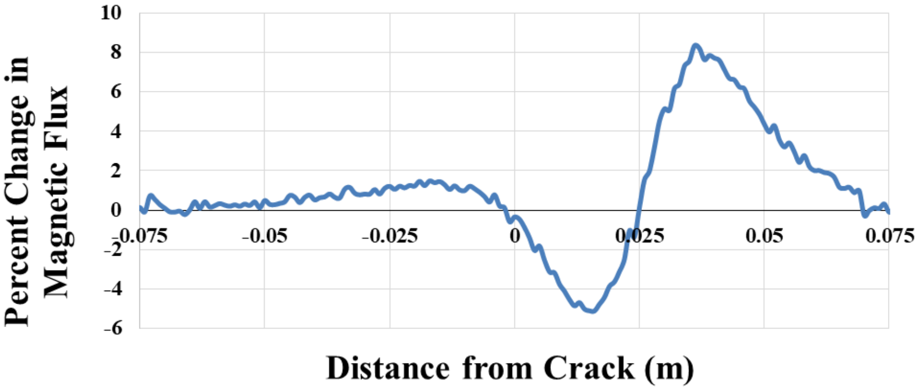

Figure 39. Changing the sensor location alters the detected change in the magnetic field. Changing the sensor location relative to the magnet allows for more thorough searches for internal cracks.

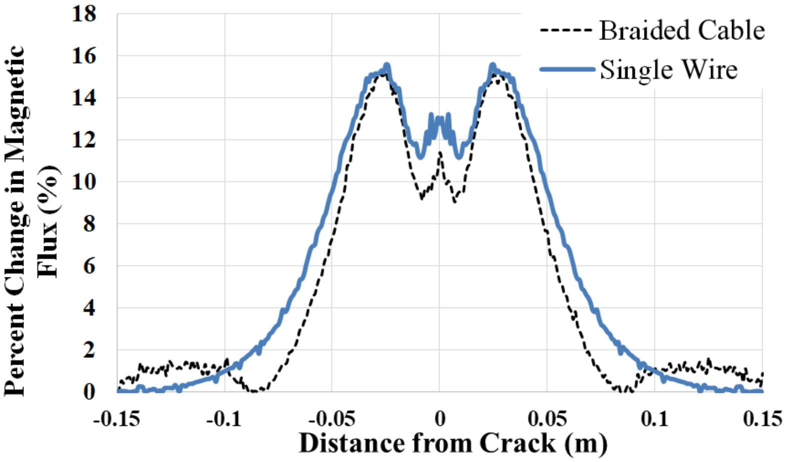

Figure 40. The magnetic flux near an internal crack shows a similar maximum change with a slightly more distinct profile in the braided cable model when compared to the single wire model with the same cross-sectional area.

6. CONCLUSIONS

The major conclusions of the project can be summarized as follows:

6.1. Fabrication and Characterization of Fe-SMA Wires and Braided Cables

6.1.1. Fabrication of Fe-SMA Wires and Braided Cables

1. A thermomechanical process was developed to enable wire drawing of FeMnAlNi at room temperature.
2. An abnormal grain growth technique was established that provides full recoverable super-elasticity by eliminating grain boundary constraints.
3. A preliminary design of atmosphere-controlled quartz furnace was completed in order to produce longer length wires necessary for wire braiding.
4. A fully functional laboratory scale wire braiding experimental test setup was designed and fabricated.
5. A 1x7 pattern Fe-SMA cable is successfully produced. It is possible to produce cables with variable diameters and configurations using the braiding test setup.

6.1.2. Characterization of Mechanical Properties of Fe-SMA Wires and Cables

1. Mechanical property control through nano-precipitation method was developed. By increasing nano-precipitate size, it is possible to increase super-elastic stress levels from 100 MPa to 600MPa. These stress levels are similar yielding stress of conventional stainless-steel cables.
2. Mechanical and super-elastic properties of the Fe-SMA cables are measured using cyclic tests. It is shown that 6.7% fully recoverable strain is achieved with 200 ºC 24h precipitation heat treatment.
3. A grip with semi-cylindrical grooves were designed and fabricated for cable testing. Grooved design increases the contact area between grip and the specimen and prevent slipping during testing at high stress levels.
4. Stainless steel and NiTi cables were tested with 1% strain increments until failure. It was shown that stainless steel cable yields around 410MPa and critical transformation stress level of NiTi cable is 520 MPa.

6.1.3. Demonstration of SHM Capability

1. An experimental test setup attachment for measuring magnetic changes in the braided cables under load was designed and fabricated. Attachment includes calibrated high-resolution hall sensor for measuring changes in the magnetic response of the material, a permanent magnet to fully saturate the parent phase of the cable. Attachment has also a capability to move up and down throughout the whole gauge length of the wire allowing to measure magnetic changes at different locations.
2. A MATLAB code was developed for data processing and a LabVIEW program was written for controlling the magnetic setup.
3. Magneto-mechanical response of Fe-SMA super-elastic wire was measured with magnetic setup. Changes in the magnetic response of Fe-SMA wire under load directly correlated with the deformation applied to the wire.

6.2. Magneto-Mechanical Finite Element Modeling

1. The Abaqus model shows how the solid mechanics of a crack propagating past an MSMA wire lead to a noticeable local phase transformation. The MSMA wire near the crack tip will transform under significant loading into martensite, allows for external sensing using a permanent magnet and sensor to measure magnetic flux.
2. To measure magnetic flux, the phase transformation was inputted into COMSOL to simulate a non-destructive evaluation of the same wire using external magnetic sensing. As the permanent magnet and sensor were moved down the length of wire along opposite sides of the concrete block, the magnetic field changes near the phase transformation.
3. For the single wire modeled in Abaqus, there is nearly a 4% change in the magnetic flux near the crack. Implementing a 1x7 braided cable created from the previous single wires in place of one single wire does not create a significant change in recorded magnetic flux change when accounting for the change in cross-sectional area. However, an increase in cross sectional area increases the maximum change in magnetic flux from 4% to over 15%, which matches with the correlation between magnetic sensitivity and MSMA wire radius.
4. The magnet and sensor location combined with the magnetic flux profile along the MSMA wire provide evidence of internal cracks near the wire under large loading.
5. The framework and initial results presented support the feasibility of SHM using MSMAs for magnetic sensing.

7. RECOMMENDATIONS

Based on the experimental and modeling results presented, it would appear that the Fe-SMA system can be realistically applied for autonomous structural sensing applications in transportation infrastructure. However, challenges remain for the economical implementation for the devices. The following recommendations address potential ways toward meeting these challenges, and toward broader commercial adoption of the technology:

1. The sensory equipment should be insulated from large changes in the magnetic environment during operation: while it acceptable to expose the sensory instrument to large external magnetic field, the sensing element depends on the change in the magnetic response: it is desirable to avoid large unplanned changes in the magnetic environment, which may require re-calibration of the instrument.
2. In order to maximize signal strength, the design should allow the sensor to be placed to the Fe-SMA wire/cable as closely as possible.
3. The corrosion resistance of the Fe-SMA material should be characterized in greater detail.
4. Calibration should also be performed on the actual structure with the embedded Fe-SMAs, not on a model or lab prototype to account for variability during construction.
5. It is important to make sure that the personnel responsible for monitoring and inspection is properly trained to understand smart materials and system in order to anticipate and properly interpret unexpected changes in the magnetic signal.

REFERENCES

1. Omori T, Ando K, Okano M, Xu X, Tanaka Y, Ohnuma I, Kainuma R, Ishida K (2011). “Superelastic effect in polycrystalline ferrous alloys.” Science, 333, 68.

2. Tanaka Y, Himuro Y, Kainuma R, Sutou Y, Omori T, Ishida K (2010). “Ferrous polycrystalline shape-memory alloy showing huge superelasticity.” Science, 327, 1488.

3. Ma J, Karaman I (2010). “Expanding the repertoire of shape memory alloys.” Science, 327, 1468.

4. Zafar, A. and Andrawes, B., “Experimental flexural behavior of sma-frp reinforced concrete beam,” Frontiers of Structural and Civil Engineering 7, Dec. 2013, pp. 341–355.

5. Tseng, L. W., Ma, J., Wang, S. J., Karaman, I., Kaya, M., Luo, Z. P., and Chumlyakov, Y. I., “Superelastic response of a single crystalline FeMnAlNi shape memory alloy under tension and compression,” Acta Materialia 89, May 2015, pp. 374–383.

6. Simonen, J. T., Andringa, M. M., Grizzle, K. M., Wood, S. L., and Neikirk, D. P., “Wireless sensors for monitoring corrosion in reinforced concrete members,” 5391, International Society for Optics and Photonics, July 2004, pp. 587–597.

7. Popovics, J. S., Gallo, G. E., Shelton, M., and Chapman, P. L., “A magnetic sensing approach to characterize corrosion in reinforced concrete,” 6529, 65291A, International Society for Optics and Photonics, Apr. 2007.

8. Bielefeldt, B. R., Benzerga, A. A., and Hartl, D. J., “Analysis of shape memory alloy sensory particles for damage detection via substructure and continuum damage modeling,” 9800, 98000B, International Society for Optics and Photonics, Apr. 2016.

9. Tseng LW, Ma Ji, Hornbuckle BC, Karaman I, Thompson GB, Luo ZP, Chumlyakov YI (2015). “The effect of precipitates on the superelastic response of [100] oriented FeMnAlNi single crystals under compression.” Acta Materialia, 97, 234-244.

10. Tseng LW, Vollmer M, Karaman I, Niendorf T, Chumlyakov YI (2015). “Effect of grain size on the superelastic response in FeMnAlNi polycrystalline alloy under tension.” Scripta Materialia 125, 68-72.

11. Tseng LW, Ma Ji, Wang SJ, Karaman I, Kaya M, Luo ZP, Chumlyakov YI (2015). “Superelastic response of a single crystalline FeMnAlNi shape memory alloy under tension and compression.” Acta Materialia, 89, 374-383.

12. Ma J, Kockar B, Evirgen A, Karaman I, Luo ZP, Chumlyakov, YI (2012). “Shape Memory Behavior and Tension-Compression Asymmetry of a Novel FeNiCoAlTa Single Crystalline Shape Memory Alloy.” Acta Materialia, 60, 2186.

13. Ma Ji, Hornbuckle BC, Karaman I, Thompson GB, Luo ZP, Chumlyakov YI. The effect of nanoprecipitates on the superelastic properties of FeNiCoAlTa shape memory alloy single crystals. Acta materialia 2013;61(9):3445-3455.Evirgen A, Ma J, Karaman I, Luo ZP,

Chumlyakov YI. Effect of aging on the superelastic response of a single crystalline FeNiCoAlTa shape memory alloy. Scripta materialia 2012;67(5):475-478.

14. Tseng LW, Ma Ji, Karaman I, Wang SJ, Chumlyakov YI. Superelastic response of the FeNiCoAlTi single crystals under tension and compression. Scripta mater 2015; 101:1-4.

15. Ozcan H, Ma Ji, Wang SJ, Karaman I, Chumlyakov Y, Brown J, Noebe RD. Effects of cyclic heat treatment and aging on superelasticity in oligocrystalline Fe-Mn-Al-Ni shape memory alloy wires. Scripta materialia 2017; 134:66-70.

16. E. Peraza-Hernandez, B. Kiefer, D. Hartl, A. Menzel, D. Lagoudas, Analytical Investigation of Structurally Stable Configurations in Shape Memory Alloy-Actuated Plates, International Journal of Solids and Structures, Vol. 69–70, pp. 442–458, 2015

17. D. Hartl, G. Chatzigeorgiou, D. Lagoudas, Three-Dimensional Modeling and Numerical Analysis of Rate-Dependent Irrecoverable Deformation in Shape Memory Alloys, International Journal of Plasticity, Vol. 26, No. 10, pp. 1485–1507, 2010.

18. D. Lagoudas, D. Hartl, Y. Chemisky, L. Machado, P. Popov, Constitutive Model for the Numerical Analysis of Phase Transformation in Polycrystalline Shape Memory Alloys, International Journal of Plasticity, Vol. 32–33, pp. 155–183, 2012.

19. G. Scalet, E. Boatti, M. Ferraro, V. Mercuri, D. Hartl, F. Auricchio, “Explicit Finite Element Implementation of a Shape Memory Alloy Constitutive Model and Associated Analyses,”

20. B. Bielefeldt, J. Hochhalter, D. Hartl, “Computationally Efficient Analysis of SMA Sensory Particles Embedded in Complex Aerostructures Using a Substructure Approach,” In Proceedings of ASME Smart Materials Adaptive Structures and Intelligent Systems (SMASIS) Conference, Colorado Spring, CO, Sept. 21–23, 2015.

21. Kiefer, B., Karaca, H., Lagoudas, D., and Karaman, I., “Characterization and modeling of the magnetic field-induced strain and work output in Ni2MnGa magnetic shape memory alloys,” Journal of Magnetism and Magnetic Materials, 2007. Vol. 312, No. 1, p. 164-176.

22. Karaman I, Basaran B, Karaca HE, Karsilayan AI, Chumlyakov YI (2007). “Energy harvesting using martensite variant reorientation mechanism in a NiMnGa magnetic shape memory alloy.” Applied Physics Letters 90, 172505.

23. Broekaart, D., “Modelling crack propagation using xfem,” (Mar. 2017) https://info.simuleon.com/blog/modelling-crack-propagation-using-xfem.

24. Lagoudas, D., Hartl, D., Chemisky, Y., Machado, L., and Popov, P., “Constitutive model for the numerical analysis of phase transformation in polycrystalline shape memory alloys,” International Journal of Plasticity 32-33, 155 – 183 (2012).

25. Hartl, D. and Lagoudas, D., “Characterization and 3-D modeling of Ni60Ti SMA for actuation of a variable geometry jet engine chevron,” Proceedings of the SPIE - The International Society for Optical Engineering 6529, 65293Z (12 pp.) – (2007//).

26. Peraza Hernandez, E., Hartl, D., and Malak, R., [Design and numerical analysis of an SMA mesh-based self-folding sheet, vol. 22 (Aug. 2013). DOI: 10.1088/0964-1726/22/9/094008.